EUROPEAN ORGANISATION FOR NUCLEAR RESEARCH (CERN)

Submitted to: JHEP

CERN-EP-2022-240
14th December 2022

Measurements of $Z\gamma$+jets differential cross sections in pp collisions at $\sqrt{s}$ = 13 TeV with the ATLAS detector

The ATLAS Collaboration

Differential cross-section measurements of $Z\gamma$ production in association with hadronic jets are presented, using the full 139 fb^{-1} dataset of $\sqrt{s}$ = 13 TeV proton–proton collisions collected by the ATLAS detector during Run 2 of the LHC. Distributions are measured using events in which the Z boson decays leptonically and the photon is usually radiated from an initial-state quark. Measurements are made in both one and two observables, including those sensitive to the hard scattering in the event and others which probe additional soft and collinear radiation. Different Standard Model predictions, from both parton-shower Monte Carlo simulation and fixed-order QCD calculations, are compared with the measurements. In general, good agreement is observed between data and predictions from MATRIX and MiNNLO$_{\text{PS}}$, as well as next-to-leading-order predictions from MadGraph5_aMC@NLO and Sherpa.

1 Introduction

Precision measurements of cross sections for the production of a Z boson and a photon ($Z\gamma$) at the Large Hadron Collider (LHC) [1] play a crucial role in the study of the Standard Model (SM) and are sensitive to physics beyond the SM. Differential cross sections for $Z\gamma$ in association with jet activity ($Z\gamma$+jets) can be used to test fixed-order perturbative QCD (pQCD) calculations and predictions with resummation of Sudakov logarithms [2]. This process is also sensitive to the parton distribution functions (PDFs) and can validate those PDFs extracted in global analyses [3]. In addition, the $Z\gamma$+jets differential cross sections can be used to constrain the Monte Carlo (MC) models, especially the parton-shower (PS) approximation [4].

In phase-space regions where the transverse momentum (p_{T}) of the system is much smaller than the mass (m) of the Z boson or $Z\gamma$, fixed-order QCD calculations are dominated by Sudakov-logarithm terms, due to soft and collinear emission, of the order of $\alpha_{\mathrm{s}}^{n} \ln^{n+1}(p_{\mathrm{T}}/m)$, where n is the fixed order considered. These terms are usually treated by resummation [5, 6] and can give very precise predictions with next-to-leading logarithms (NLL) and up to next-to-next-to-next-to-leading logarithms (N3LL) [2]. These resummation models can be tested in phase-space regions where the logarithm terms dominate, i.e. in regions where the hard scale of the process is much larger than the value of the observable considered.

Such a phase-space region can be probed by simultaneously measuring two independent observables, providing a more complete description of the pattern of QCD emission [7]. This is done with two-dimensional (2D) distributions, measuring an observable sensitive to the hard scale, called the *hard variable*, as a function of another observable, called the *resolution variable*, which probes the additional soft radiation. Thus, the *hard variable* is an observable which is directly sensitive to the hard scale of the process and its value is non-zero at leading order (LO), e.g. p_{T}^{Z} , p_{T}^{γ}, $m_{Z\gamma}$, or any linear combinations of these variables. On the other hand, a *resolution variable* is an observable sensitive to the additional soft or collinear QCD radiation; the values of these observables, e.g. $p_{\mathrm{T}}^{Z\gamma}$ or N_{jet}, are zero at LO and take non-zero values only beyond LO. An example of a 2D measurement is the differential cross section as a function of $p_{\mathrm{T}}^{Z} - p_{\mathrm{T}}^{\gamma}$ in different regions of $p_{\mathrm{T}}^{Z} + p_{\mathrm{T}}^{\gamma}$. In these measurements, $p_{\mathrm{T}}^{Z} - p_{\mathrm{T}}^{\gamma}$ is the *resolution variable* that allows effects near the Jacobian peak to be studied, whereas $p_{\mathrm{T}}^{Z} + p_{\mathrm{T}}^{\gamma}$ is the *hard variable* that tests the different scales [6].

Measurements of $Z\gamma$ production have been performed by experiments at LEP [8–10], the Tevatron [11, 12], and the LHC [13–15]. However, no new physics or deviations from the predictions of the SM have been observed. An example of physics beyond the SM is given by the model that includes axion-like particles (ALPs) [16], which is particularly relevant for $Z\gamma$ production; these particles were introduced to solve the strong CP problem and are also considered as a dark-matter candidate [17]. Measurements of $Z\gamma$ production can help to constrain the ALP's couplings to the Z boson and the photon [18], which define the most general CP-conserving Lagrangian describing the ALP's bosonic interactions [19]. Another case where $Z\gamma$ production can help is in the use of effective field theory [20]. These models describe different theories beyond the SM that introduce new-physics states at a mass scale Λ that is large in comparison with the electroweak scale, using gauge-invariant combinations of SM fields. Previous measurements have not found any evidence of new physics in the $Z\gamma$ final state. However, none of these measurements included any dedicated study of jet activity. Requiring the presence of jets in addition to the $Z\gamma$ pair, leads to configurations in the final state that enhance a region of the phase space different than that studied in the case of inclusive production. Therefore, measurements of differential cross sections for $Z\gamma$+jets production are expected to provide additional sensitivity to constrain ALPs and other models for physics beyond the SM.

This paper presents measurements of differential cross sections as functions of QCD-related observables associated with the $Z\gamma$+jets process. The measurements are performed differentially in either one or two observables. The analysis uses the full dataset of proton–proton (pp) collisions at a centre-of-mass energy of $\sqrt{s}$ = 13 TeV recorded by the ATLAS detector during Run 2 (2015–2018) of the LHC. The results presented here build upon a previous analysis performed by ATLAS [14], which focused on more inclusive observables. The measurements extend the published results by including the hadronic activity associated with the $Z\gamma$ system and by measuring double-differential cross sections.

As in the previous analysis, only Z bosons decaying into pairs of charged leptons ($\ell^+\ell^-$, with $\ell = e, \mu$) are considered. This restriction makes it easier to fully reconstruct the final state with high resolution, and also provides a relatively large cross section with little background. Events are selected by requiring the invariant mass of the two leptons ($m_{\ell\ell}$) to be greater than 40 GeV, and the sum of the mass of the dilepton system and the mass of the $\ell\ell\gamma$ system ($m_{\ell\ell} + m_{\ell\ell\gamma}$) to be greater than 182 GeV. These selections define a phase space that is enriched in photons from initial-state radiation (ISR), such as shown in Figure 1(a). In addition, these requirements reduce the contribution from final-state radiation (FSR), where the photons are radiated from the leptons as shown in Figure 1(b). In the $m_{\ell\ell}$ vs $m_{\ell\ell\gamma}$ plane, the second requirement forms a diagonal straight line that separates FSR events from ISR events; this is because the FSR events are expected to lie in the region with $m_{\ell\ell\gamma}$ around the nominal Z boson mass, with $m_{\ell\ell}$ at lower values.

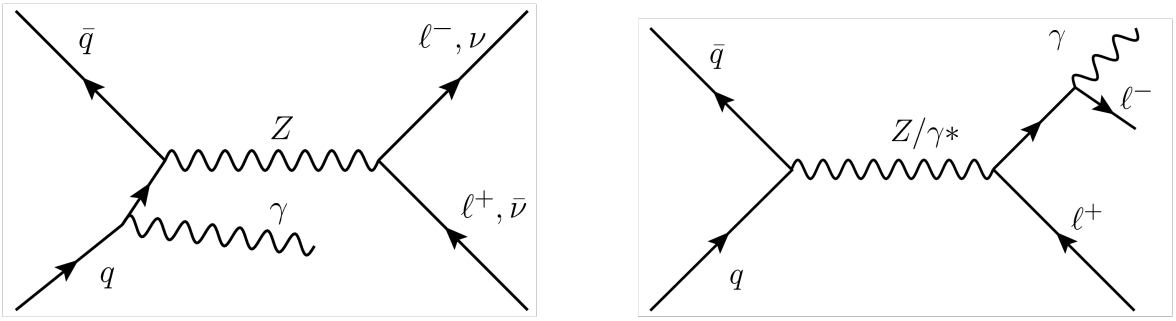

(a) (b)

Figure 1: Diagrams for (a) $Z\gamma$ production via the ISR process and (b) $\ell\ell\gamma$ production via the FSR process.

The predictions of several MC models for $Z\gamma$ production, which include multileg matrix elements interfaced with parton-shower and hadronisation approximations, are compared with the measurements. Several models, which have different levels of precision, are considered: Sherpa 2.2.4 [21] at LO and Sherpa 2.2.11 [21] at next-to-leading order (NLO), MadGraph at NLO [22] and MiNNLO$_{\text{PS}}$ at NNLO [23, 24]. The predictions of the fixed-order QCD calculations by MATRIX [25, 26] at NNLO are also compared with the data.

2 The ATLAS detector

The ATLAS experiment [27] at the LHC is a multipurpose particle detector with a forward–backward symmetric cylindrical geometry and a near 4π coverage in solid angle.[1] It consists of an inner tracking

[1] ATLAS uses a right-handed coordinate system with its origin at the nominal interaction point (IP) in the centre of the detector and the z-axis along the beam pipe. The x-axis points from the IP to the centre of the LHC ring, and the y-axis points upwards. Cylindrical coordinates (r, ϕ) are used in the transverse plane, ϕ being the azimuthal angle around the z-axis.

detector (ID) surrounded by a thin superconducting solenoid providing a 2 T axial magnetic field, electromagnetic and hadron calorimeters, and a muon spectrometer (MS). The inner tracking detector covers the pseudorapidity range $|\eta| < 2.5$. It consists of silicon pixel, silicon microstrip, and transition radiation tracking detectors. Lead/liquid-argon (LAr) sampling calorimeters provide electromagnetic (EM) energy measurements with high granularity. A steel/scintillator-tile hadron calorimeter covers the central pseudorapidity range ($|\eta| < 1.7$). The endcap and forward regions are instrumented with LAr calorimeters for both the EM and hadronic energy measurements up to $|\eta| = 4.9$. The muon spectrometer surrounds the calorimeters and is based on three large superconducting air-core toroidal magnets with eight coils each. The field integral of the toroids ranges between 2.0 and 6.0 T m across most of the detector. The muon spectrometer includes a system of precision tracking chambers and fast detectors for triggering. A two-level trigger system is used to select events. The first-level trigger is implemented in hardware and uses a subset of the detector information to accept events at a rate below 100 kHz. This is followed by a software-based trigger that reduces the accepted event rate to 1 kHz on average depending on the data-taking conditions. An extensive software suite [28] is used in data simulation, in the reconstruction and analysis of real and simulated data, in detector operations, and in the trigger and data acquisition systems of the experiment.

3 Data and simulated samples

The data used in this analysis were obtained from pp collisions produced by the LHC in Run 2, and after applying the data quality criteria [29], the total integrated luminosity recorded by the ATLAS detector is 139 fb^{-1}. The uncertainty in the luminosity is 1.7% [30], obtained from measurements with the LUCID-2 detector [31].

Three different Monte Carlo samples are used to simulate the $Z\gamma$+jets process. The nominal sample was generated using the program Sherpa 2.2.11 to calculate matrix elements with up to one additional parton at NLO and up to three additional partons at LO. The matrix element calculation includes all diagrams at order α_{EW}^2, where α_{EW} is the electroweak coupling constant. The merging of the matrix element and parton shower (PS) was performed with MEPS@LO [32–35]. The NNPDF3.0nnlo [36] PDF set was used, with an additional set of tuned PS parameters developed by the Sherpa authors. Frixione isolation [37] was applied to the photon with the parameter choices $\delta_0 = 0.1$, $\epsilon = 0.1$ and $n = 2$. This sample requires the transverse momentum of the photon (p_{T}^{γ}) to be greater than 7 GeV. Throughout the paper the signal estimate refers to this sample, unless it is otherwise specified.

A second sample was produced using the program Sherpa 2.2.4, with matrix elements at LO accuracy in QCD for up to three additional parton emissions matched and merged with the Sherpa parton shower based on Catani–Seymour dipole factorisation [38, 39] using the MEPS@LO prescription [32–35]. The matrix element calculation includes all diagrams at order α_{EW}^2. Samples were generated using the NNPDF3.0nnlo PDF set [40], along with the dedicated set of tuned parton-shower parameters developed by the Sherpa authors. In the generation, p_{T}^{γ} is required to be larger than 7 GeV. Frixione isolation was also applied to this sample, with the same parameter values as in the Sherpa 2.2.11 sample.

A third sample was generated using the program MadGraph5_aMC@NLO 2.3.3 [22] to calculate NLO matrix elements with up to one extra parton, using the NNPDF3.0nlo_as_0118 PDF set [40]. The matrix

The pseudorapidity is defined in terms of the polar angle θ as $\eta = -\ln\tan(\theta/2)$. Angular distance is measured in units of $\Delta R \equiv \sqrt{(\Delta y)^2 + (\Delta\phi)^2}$, where y is the rapidity, defined as $y = (1/2)\ln[(E + p_z)/(E - p_z)]$.

element calculation includes all diagrams at order α_{EW}^2. This sample has the same Frixione isolation parameter values as in the SHERPA samples.

Simulated samples of the purely electroweak production of $Z\gamma$ in association with two jets are used at detector level. These samples were generated using the program MADGRAPH5_AMC@NLO 2.6.5 [22] at LO accuracy in α_{EW}^4, using the NNPDF3.0LO PDF set [40]. It was interfaced with PYTHIA 8.240 [41] for parton showering, hadronisation, and the underlying event.

The main backgrounds to the signal arise from Z bosons produced in association with jets, from top-quark pairs and single top quarks produced in association with photons, from diboson and triboson events, and from multiple pp interactions; the last of these are called pile-up events in the following.

The Z boson in association with jets (Z + jets) MC samples used in this analysis were generated using the POWHEG BOX v1 MC generator [42–45], with NLO accuracy for the hard-scattering processes. It was interfaced to PYTHIA 8.186 [41] for the modelling of the PS, hadronisation, and underlying events, with parameters values set according to the AZNLO tune [46]. The CT10NLO PDF set [47] was used for the hard-scattering processes, whereas the CTEQ6L1 PDF set [48] was used for the PS. This background is normalised to the cross section given by the generator.

The MC samples of the production of one or two top quarks and a photon ($t\bar{t}\gamma$ and $tW\gamma$) were generated using the program MADGRAPH5_AMC@NLO 2.3.3 [22] at LO with the NNPDF2.3LO [40] PDF set. The events were interfaced with PYTHIA 8.212 [49] using the ATLAS A14 tune [50] and the NNPDF2.3LO PDF set. These samples are normalised to their NLO cross section [51, 52].

The MC samples of diboson processes, such as $ZZ \to \ell\ell\ell\ell$ and $W^{\pm}Z \to \ell\ell\ell\nu$, were generated with SHERPA 2.2.2 with matrix elements at NLO accuracy in QCD for up to one additional parton and at LO accuracy for up to three additional parton emissions. The matrix element calculations were matched and merged with the SHERPA parton shower based on Catani–Seymour dipole factorisation [38, 39] using the MEPS@NLO prescription [32–35]. The virtual QCD corrections were provided by the OPENLOOPS library [53–55]. The NNPDF3.0NNLO set of PDFs was used [40], along with the dedicated set of tuned parton-shower parameters developed by the SHERPA authors.

The $WZ\gamma$ and $WW\gamma$ processes constitute a small background and were simulated with SHERPA 2.2.11 at NLO with zero jets, using the NNPDF3.0NNLO PDF set. The multiboson background samples are normalised to the cross section given by the generator.

For all these MC samples, pile-up from additional pp collisions in the same and neighbouring bunch crossings was simulated by overlaying each MC event with a variable number of simulated inelastic pp collisions generated using PYTHIA 8.186 with the ATLAS set of tuned parameters for minimum-bias events (the A3 tune) [56]. The MC events are weighted ('pile-up reweighting') to reproduce the distribution of the average number of interactions per bunch crossing observed in the data.

All the samples of generated events were passed through the GEANT4-based [57] ATLAS detector- and trigger-simulation programs [58]. They are reconstructed and analysed by the same program chain as the data. Table 1 gives an overview of the generators used in this analysis, their precision in QCD, and the PDF set used.

Additional signal theory predictions at NNLO matched to the parton shower [24] were calculated using POWHEG BOX [59]. They provide a prediction consistently matched to the parton shower, including spin correlation, intereference and off-shell effects, using the MiNNLO$_{\mathrm{PS}}$ [23] approach. These predictions are compared with the data in Section 9. Photon infrared-safe predictions were obtained by imposing the

Table 1: Summary of MC samples used in the analysis.

Process	Generator	Order	PDF set	PS/UE/MPI
$Z\gamma$+jets	Sherpa 2.2.11	0,1j@NLO + 2,3,4j@LO	NNPDF3.0nnlo	Sherpa 2.2.11
$Z\gamma$+jets	Sherpa 2.2.4	0,1,2,3j@LO	NNPDF3.0nnlo	Sherpa 2.2.4
$Z\gamma$+jets	MadGraph5_aMC@NLO	0,1j@NLO	NNPDF3.0nlo_as_0118	Pythia 8.212
Purely EW Zjj	MadGraph5_aMC@NLO	LO	NNPDF3.0lo	Pythia 8.240
Z + jets	Powheg Box	0j@NLO	CT10nlo	Pythia 8.186
$t\bar{t}\gamma, tW\gamma$	MadGraph5_aMC@NLO	LO	NNPDF2.3lo	Pythia 8.212
$ZZ \to \ell\ell\ell\ell, W^{\pm}Z \to \ell\ell\ell\nu$	Sherpa 2.2.2	0,1j@NLO + 2,3j@LO	NNPDF3.0nnlo	Sherpa 2.2.2
$WZ\gamma, WW\gamma$	Sherpa 2.2.11	0j@NLO + 1,2j@LO	NNPDF3.0nnlo	Sherpa 2.2.11

same Frixione isolation parameter values as for the Sherpa 2.2.11 sample. The central renormalisation and factorisation scales were set to $m_{\ell\ell\gamma}$. Events were generated using the NNPDF3.0nnlo PDF set with the strong coupling constant taken as $\alpha_s(m_Z) = 0.118$.

Fixed-order QCD calculations are also considered by using the program MATRIX [25, 26], which relies on OpenLoops [54] for all amplitudes up to the one-loop level, and on other dedicated calculations [55, 60–62]. The MATRIX predictions are obtained with CT14nnlo PDFs [63]. Frixione isolation parameter values are the same as for the Sherpa 2.2.11 sample. The MATRIX predictions are obtained at Born level (parton level), since no QED radiation is present, whereas the measurements are at particle level. For this reason, corrections are applied to the fixed-order calculations. These corrections are calculated by comparing Born-level leptons with *dressed* leptons. Dressed leptons are corrected for collinear photon radiation by adding to the four-momentum of the lepton the four-momenta of those photons, not coming from hadronic decays, which are within $\Delta R = 0.1$ of the lepton. Since MATRIX does not include non-perturbative effects, corrections are applied to allow comparisons with the measurements. These corrections are obtained by calculating the ratio of the MC cross sections with and without hadronisation. The MC sample used for these corrections was generated with MadGraph5_aMC@NLO with up to one extra parton at NLO in the matrix element, and then interfaced with Pythia 8 [49], using the A14 tune [50].

4 Event selection

Selected events must have at least one reconstructed vertex with at least two associated tracks with $p_T > 500$ MeV. In events with multiple vertices, the one with the highest $\sum p_T^2$ of associated tracks is selected as the primary vertex. Candidate events must also pass at least one unprescaled single-muon or single-electron trigger [64, 65]. For data recorded in 2015, the lowest p_T threshold was 24 GeV for the electron trigger, and 20 GeV for the muon trigger. For data recorded during the period 2016−2018, these thresholds were both raised to 26 GeV and tighter isolation criteria were applied, to compensate for the increase in instantaneous luminosity. Triggers with a higher p_T threshold, but looser isolation, are also used because they increase the total trigger efficiency.

4.1 Lepton, photon, and jet selections

Photons and electrons are reconstructed from energy clusters in the electromagnetic calorimeter (ECAL). Electron candidates are required to have a matching track in the ID. Photon candidates must have $|\eta| < 2.37$ and $p_T > 30$ GeV, while electron candidates must have $|\eta| < 2.47$ and $p_T > 25$ GeV. Both electron

and photon candidates are rejected if they lie in the transition region between the barrel and endcaps of the ECAL ($1.37 < |\eta| < 1.52$). Electrons are identified using a likelihood function based on shower shape variables in the ECAL, track variables, and the quality of the track–cluster matching. Electrons are required to satisfy the *Medium* criteria, as described in Ref. [66]. Photons are identified using shower shape variables in the ECAL and are required to satisfy the *Tight* criteria [66]. Photons are classified as *converted* to electron–positron pairs if the ECAL cluster is matched to a conversion vertex formed by the tracks of oppositely charged particles, or by a single track consistent with having originated from a photon conversion. Photon candidates are classified as *unconverted* if it is not possible to match clusters to tracks. Both types of photons are used in this analysis, and the distinction between converted and unconverted photons has no impact on the result. The photon and electron energy scale is calibrated using $Z \to ee$ events, as described in Ref. [66].

Muons are reconstructed by matching the tracks in the MS with tracks in the ID. The momentum is obtained by combining the MS measurement, corrected for the energy deposited in the calorimeter, and the measurement in the ID. Muon candidates are also required to satisfy the *Medium* identification criterion, as described in Ref. [67]. This criterion is based on the number of hits matched to the muon's tracks reconstructed in the ID and the MS, and on the compatibility of the ID and MS measurements of the muon's transverse momentum. Muon candidates are required to have $|\eta| < 2.5$ and $p_{\mathrm{T}} > 25$ GeV.

Electrons and muons must be compatible with originating from the primary vertex. This requirement is fulfilled by requiring that the transverse impact parameter (d_0) relative to the beam-spot divided by its uncertainty ($\sigma(d_0)$), i.e. the significance, satisfy $|d_0/\sigma(d_0)| < 5$ for electrons and $|d_0/\sigma(d_0)| < 3$ for muons. Additionally, for both electrons and muons, the longitudinal impact parameter (z_0), i.e. the z-distance from the primary vertex to the point where d_0 is measured, must satisfy $|z_0 \sin\theta| < 0.5$ mm.

Leptons and photons are required to be isolated, i.e. without additional activity in their proximity. Isolation requirements are based on tracking information and calorimeter energy clusters. The isolation variable $p_{\mathrm{T}}^{\mathrm{iso}}$ is computed as the $\sum p_{\mathrm{T}}$ of nearby tracks with $p_{\mathrm{T}} > 1$ GeV, excluding tracks associated with the lepton or photon candidate. The variable $E_{\mathrm{T}}^{\mathrm{iso}}$ is obtained as the scalar sum of the transverse energies of nearby topological clusters, corrected for the energy deposited by the photon or lepton candidate itself and the contribution from the underlying event and pile-up [68, 69].

Photons must satisfy an isolation criterion, as described in Ref. [66], with $p_{\mathrm{T}}^{\mathrm{iso}}/E_{\mathrm{T}} < 0.05$ and $E_{\mathrm{T}}^{\mathrm{iso}}/E_{\mathrm{T}} < 0.065$ in a cone of size $\Delta R = 0.2$ around the photon candidate. Electrons must satisfy $p_{\mathrm{T}}^{\mathrm{iso}}/p_{\mathrm{T}} < 0.15$ in a cone of p_{T}-dependent size up to $\Delta R = 0.2$ around the electron candidate, and $E_{\mathrm{T}}^{\mathrm{iso}}/p_{\mathrm{T}} < 0.2$ in a cone of size $\Delta R = 0.2$. Muon isolation [67] requires $p_{\mathrm{T}}^{\mathrm{iso}}/p_{\mathrm{T}} < 0.15$ in a cone of p_{T}-dependent size up to $\Delta R = 0.3$ ($\Delta R = 0.2$) for muons with p_{T} less (greater) than 50 GeV, and $E_{\mathrm{T}}^{\mathrm{iso}}/p_{\mathrm{T}} < 0.3$ in a cone of fixed size $\Delta R = 0.2$.

Jets are reconstructed with the anti-k_t algorithm [70, 71] with a radius parameter of $R = 0.4$, using a particle-flow [72] procedure, with clusters of energy deposited in the calorimeter as inputs. Jets are calibrated and their energy is corrected to account for detector effects, using methods based on MC and in-situ techniques [73]. Pile-up jets are removed when identified with the jet vertex tagger (JVT) [74], using the *Medium* working point applied to all jets with $p_{\mathrm{T}} < 60$ GeV and $|\eta| < 2.4$. Jets are required to have $p_{\mathrm{T}} > 30$ GeV if $|\eta| < 2.5$, or $p_{\mathrm{T}} > 50$ GeV if $|\eta| > 2.5$, to further suppress pile-up. Distributions with jets require at least one jet, unless it is otherwise explicitly stated.

Ambiguities in the identity of reconstructed leptons, jets, and photons are resolved with an overlap-removal procedure. First, jets are removed if they are within $\Delta R = 0.4$ of a photon, or within $\Delta R = 0.2$ of an

electron. Then leptons are removed if they are within $\Delta R = 0.4$ of a jet, while photons are removed if they are within $\Delta R = 0.4$ of a lepton. Finally, electrons are removed if they are within $\Delta R = 0.2$ of a muon.

4.2 Signal region and control region definitions

The signal region (SR) is defined by events with at least two opposite-sign (OS) same-flavour (SF) leptons and a photon. The leading lepton (with the highest transverse momentum) is required to have $p_{\mathrm{T}} > 30$ GeV. Events must also have at least one photon with $p_{\mathrm{T}}^{\gamma} > 30$ GeV. Events are further selected by requiring $m_{\ell\ell} > 40$ GeV, to avoid low-mass resonances. As mentioned in Section 1, FSR events are suppressed by requiring that the sum of the invariant mass of the leptons and the invariant mass of the leptons and the photon is greater than twice the mass of the Z boson, i.e. $m_{\ell\ell} + m_{\ell\ell\gamma} > 182$ GeV. In the $m_{\ell\ell}$ vs $m_{\ell\ell\gamma}$ plane, this requirement is a diagonal straight line that separates FSR and ISR events since FSR events are expected to lie in the region with $m_{\ell\ell\gamma} \sim 90$ GeV and $m_{\ell\ell} < 90$ GeV (see Figure 3 in Ref. [14]).

The $t\bar{t}\gamma$ background modelling is checked in a dedicated control region ($t\bar{t}\gamma$-CR) obtained by applying all of the SR requirements except the SF-lepton requirement, which is replaced by a requirement of different-flavour (DF) leptons. The signature in the $t\bar{t}\gamma$-CR is then $e\mu\gamma$. Table 2 shows a summary of these selection criteria.

Table 2: Summary of the selection criteria used in this analysis.

Observable	Signal Region	$t\bar{t}\gamma$ Control Region
Number of signal leptons	≥ 2 opposite sign, same flavour	≥ 2 opposite sign, different flavour
Lepton	$p_{\mathrm{T}}(\ell_1) > 30$ GeV, $p_{\mathrm{T}}(\ell_2) > 25$ GeV	
Photon	≥ 1 photon with $p_{\mathrm{T}}^{\gamma} > 30$ GeV	
$m_{\ell\ell}$	> 40 GeV	
$m_{\ell\ell} + m_{\ell\ell\gamma}$	> 182 GeV	

5 Measured observables

Differential cross sections are measured for the following one-dimensional observables:

- N_{jets}, the number of jets
- $p_{\mathrm{T}}^{\mathrm{jet1}}$ ($p_{\mathrm{T}}^{\mathrm{jet2}}$), the transverse momentum of the leading jet (subleading jet)
- $p_{\mathrm{T}}^{\mathrm{jet2}}/p_{\mathrm{T}}^{\mathrm{jet1}}$, the ratio of the p_{T} of the subleading jet and leading jet
- $m_{\ell\ell\gamma j}$, the invariant mass of the lepton-pair–photon–leading-jet system
- m_{jj}, the invariant mass of the two leading jets
- H_{T}, the scalar sum of the p_{T} of all jets, leptons, and photons
- $p_{\mathrm{T}}^{\gamma}/\sqrt{H_{\mathrm{T}}}$, the ratio of the p_{T} of the photon to the square root of H_{T}
- $\Delta\phi(\mathrm{jet}, \gamma)$, the azimuthal angle between the leading jet and the leading photon

- $\Delta R(\ell,\ell)$, the angular distance ΔR between the two leptons, measured in units of $\Delta R \equiv \sqrt{(\Delta\eta)^2 + (\Delta\phi)^2}$.
- $p_{\mathrm{T}}^{\ell\ell}$, the transverse momentum of the two-lepton system
- $p_{\mathrm{T}}^{\ell\ell} - p_{\mathrm{T}}^{\gamma}$, the difference between the transverse momenta of the $\ell\ell$ system ($p_{\mathrm{T}}^{\ell\ell}$) and the photon ($p_{\mathrm{T}}^{\gamma}$)
- $p_{\mathrm{T}}^{\ell\ell} + p_{\mathrm{T}}^{\gamma}$, the scalar sum of the transverse momenta of the $\ell\ell$ system and the photon
- $p_{\mathrm{T}}^{\ell\ell\gamma\mathrm{j}}$, the transverse momentum of the $\ell\ell\gamma j$ system.

The QCD-sensitive 2D observables measured in this paper are:

- The *resolution variable* $p_{\mathrm{T}}^{\ell\ell\gamma}/m_{\ell\ell\gamma}$, the ratio of the transverse momentum of the $\ell\ell\gamma$ system to its mass, is measured in bins of the *hard variable* $m_{\ell\ell\gamma}$
- The *resolution variable* $p_{\mathrm{T}}^{\ell\ell} - p_{\mathrm{T}}^{\gamma}$ is measured in three different bins of the *hard variable* $p_{\mathrm{T}}^{\ell\ell} + p_{\mathrm{T}}^{\gamma}$
- The *resolution variable* $p_{\mathrm{T}}^{\ell\ell\gamma\mathrm{j}}$ is measured in bins of the *hard variable* $p_{\mathrm{T}}^{\ell\ell\gamma}$

Additionally, 2D observables sensitive to polarisation effects of the Z boson are considered [75]:

- $\cos\theta_{\mathrm{CS}}$, the cosine of the angle between the negatively charged lepton and the lepton pair in the Collins–Soper (CS) frame [76] in bins of $p_{\mathrm{T}}^{\ell\ell}$
- ϕ_{CS}, the azimuthal angle between the negatively charged lepton and the lepton pair in the CS frame in bins of $p_{\mathrm{T}}^{\ell\ell}$.

The polarisation-sensitive observables are estimated in the Collins–Soper frame, where the Z boson is at rest; the CS frame is commonly used when extracting angular coefficients of the Z boson [77, 78].

For the 2D distributions, computational complications in the unfolding of a 2D distribution are avoided by unfolding the resolution observable in wide bins of the hard observable. These wide bins are chosen such that the migration effects in the hard observable are negligible.

6 Background estimation

The main background to the $Z\gamma$+jets signal arises from Z+jets events, in which one of the jets is misidentified as a photon. This background is estimated using a data-driven method. Pile-up events, in which the leptons and the photon originate from two different pp interactions during the same bunch crossing, also constitute a background and are estimated using a data-driven method. Another large background, especially at high jet multiplicity, is $t\bar{t}\gamma$ production, where the top-quark decays can also produce same-flavour leptons. The $t\bar{t}\gamma$ background is estimated using MC samples normalised to data in the dedicated $t\bar{t}\gamma$-CR defined in Section 6.3. Other small backgrounds that can also produce the same signature as the signal, such as triboson events from $WW\gamma$, $WZ\gamma$, and $ZZ\gamma$ production, are estimated using MC samples. The background from diboson events, such as $WZ(\rightarrow \ell\nu\ell\ell)$ and $ZZ(\rightarrow \ell\ell\ell\ell)$, where one electron is misidentified as a photon is also taken into account using MC samples.

6.1 Z + jets background

A two-dimensional sideband method [68], similar to the one in Ref. [14], is used to estimate the background in each bin of each distribution. In addition to the SR and the $t\bar{t}\gamma$-CR, three Z + jets-CRs are created to estimate this background by inverting the isolation and/or identification criteria for the photon. Photons that fail to satisfy the *Tight* identification criteria must still satisfy a loose identification criterion, where the requirements on four of the EM calorimeter shower shape variables are removed, as described in Ref. [79]. The photon isolation is modified such that only the calorimeter-based component is considered, while the track-based isolation is applied in all regions. Photon candidates fail to satisfy the isolation criteria when $E_{\mathrm{T}}^{\mathrm{iso}} > 0.065 \times E_{\mathrm{T}}^{\gamma} + E_{\mathrm{T}}^{\mathrm{gap}}$, where $E_{\mathrm{T}}^{\mathrm{gap}}$ is an energy gap set to $E_{\mathrm{T}}^{\mathrm{gap}} = 2$ GeV and helps to reduce the number of $Z\gamma$+jets signal events leaking into the Z + jets-CRs (signal leakage).

The Z + jets-CRs described above are dominated by Z + jets events. The leakage of signal events into the Z + jets-CRs is removed via the signal leakage fractions estimated using the MC simulation. These factors are inclusively about 6% (1.4%) for the control region with modified identification (isolation) criteria, and less than 0.2% for the control region where both the identification and isolation criteria are modified. Backgrounds from other processes are subtracted using the MC simulation of each process. The purity in the CR is 0.90 ± 0.02, with values varying from 0.86 to 0.92, depending on the exact bin. The yields of Z + jets events in the SR can then be derived from the number of events in the SR and in the three Z + jets-CRs, using the formulas described in Ref. [68].

Possible correlations between the isolation and identification variables are estimated with Z + jets MC samples with the use of a correlation factor R, which is the ratio of the fraction of Z + jets events satisfying the photon isolation requirement $E_{\mathrm{T}}^{\mathrm{iso}} < 0.065 \times E_{\mathrm{T}}^{\gamma}$ in events satisfying the identification criteria, to those not satisfying the identification criteria. In the absence of correlation, this ratio is equal to unity. To preserve the correlation and reduce the statistical uncertainties, R is computed in larger bins than those used in the sideband method or integrated, depending on the observable. Results of the Z + jets estimation with larger intervals for the correlation computation are compatible within uncertainties with the results with finer binning, but with reduced systematic and statistical uncertainties.

The uncertainty in the correlation factor R is obtained by varying the definition of the Z + jets-CRs in both data and MC simulation. The $E_{\mathrm{T}}^{\mathrm{gap}}$ requirement is varied by ±1 GeV and different loose identification criteria are used, for which three or five of the EM calorimeter shower shape variables are removed from the *Tight* criteria instead of four. In the inclusive phase space, the correlation factor is $R = 1.30 \pm 0.04$ (stat.) ± 0.23 (syst.), estimated using the MC samples, as mentioned above. A cross-check of this estimate is performed by computing R in a Z + jets-CR where photons also fail the track isolation, and in this CR the estimate is $R = 1.29 \pm 0.02$ (stat.), in agreement with the nominal estimate. Another source of uncertainty arises from the estimation of the $Z\gamma$+jets signal leakage into the Z + jets-CRs. The signal leakage factors are computed using Sherpa 2.2.11 and are found to be small; the uncertainty is estimated by using MadGraph instead of Sherpa. Additional uncertainties in R arise from the subtraction of other backgrounds (such as diboson events, or $t\bar{t}\gamma$). For these, the uncertainties in the cross sections are propagated to the final Z + jets estimate. The total uncertainty (including statistical uncertainties) in the integrated Z + jets estimate is 22% and is dominated by the uncertainty of the data-driven method.

6.2 Pile-up background

The selected photons may originate from different pp collisions in the same bunch crossing because photons do not have requirements on the longitudinal position of their origin (z_γ) with respect to the primary vertex, since it is not a well-measured quantity. The reconstructed photon z_γ is determined by using a weighted mean of the intersections of the directions obtained from the electromagnetic clusters by taking into account the longitudinal segmentation of the calorimeter, with a constraint from the beam-spot position, and has a typical resolution of 15 mm.

This background is estimated, using a method similar to the one described in Ref. [14], by evaluating the fraction of pile-up events in data (f_{PU}) after the $\ell\ell\gamma$ selection, and it is briefly described here. To select photons with a better position resolution $\sigma(z_\gamma)$, only photons that converted to electron–positron pairs with two tracks in the pixel detector are considered. Additionally, the radial conversion position of the photons must be between 5 mm from the beam-spot (outside the beam pipe) and 125 mm (before the end of the pixel detector). The f_{PU} of converted photons is assumed to be the same as for unconverted ones. This assumption is checked using a sample of signal MC events. In this sample, the fraction of events with 'MC truth'-matched photons is the same for events with and without photon conversion. This is expected since the two effects (i.e. pile-up fraction and conversion fraction) should not be correlated.

The primary vertex position z_{vtx} has a Gaussian distribution with a measured width of $\sigma(z_{\text{vtx}}) \sim 35$ mm [14], corresponding to the width of the luminous region. The fraction f_{PU} can then be written as:

$$f_{\text{PU}} = \frac{1}{N_{\text{data}}} \cdot \frac{N_{\text{data}}^{\text{PU}} - N_{\text{MC}}^{\text{PU}}}{P_{\text{PU}}},$$

where $N_{\text{data(MC)}}^{\text{PU}}$ is the number of data (MC) events in a region dominated by pile-up, defined as the region with $|\Delta z| = |z_{\text{vtx}} - z_\gamma| > 50$ mm. Since the pile-up events are Gaussian-distributed with a width $\sigma(z_{\text{vtx}} - z_\gamma) = \sqrt{2}\sigma(z_{\text{vtx}}) \sim 50$ mm, the probability of observing events with $|\Delta z| > 50$ mm is estimated to be $P_{\text{PU}} = 0.32$. The term N_{MC} describes the MC events where the Z boson and the photon come from the same pp collision, and is taken from signal MC simulation. The MC sample is normalised to the data with $|\Delta z| < 5$ mm. The $|z_{\text{vtx}} - z_\gamma|$ distribution is shown in Figure 3 of Ref. [14]. To have a better description of the pile-up events in the differential observables, f_{PU} is computed as a function of N_{jets} and p_{T}^γ. The estimated f_{PU} varies from 0.02 to 0.08.

The procedure described above gives the total fraction of pile-up events in bins of p_{T}^γ and N_{jets}, while the shape for the other distributions is taken from the MC samples at particle level, as described in the following. A sample is built by adding together a generated single-photon sample and a generated Z + jets sample. Only jets from the Z + jets sample are considered, since in data and MC events the jets are required to be matched to the vertex with the highest $\sum p_{\text{T}}^2$ of associated tracks through the JVT requirement, which is likely to reject the jets produced in association with the photon.

The difference between the nominal particle-level sample and a pile-up enriched sample is assigned as an uncertainty. This additional pile-up enriched sample is selected from the data, by selecting only events where z_γ is closer to the vertex with the second highest $\sum p_{\text{T}}^2$ of associated tracks than to the primary vertex. By definition, these events will be pile-up-like events. In observables that depend on jets, the difference between this particle-level distribution and the one obtained by considering all the jets is added as an additional uncertainty.

6.3 Other backgrounds

Background contributions from $t\bar{t}\gamma$, triboson, and diboson events are estimated with simulated samples. The largest contribution arises from $t\bar{t}\gamma$ processes and is around four times larger than the others, and therefore the modelling is checked in the dedicated $t\bar{t}\gamma$-CR defined in Section 4.2. The $t\bar{t}\gamma$ MC sample is scaled by a normalisation factor of 1.44, and a relative uncertainty of 15% is assigned to this normalisation [80].

Figure 2 shows a comparison between data and MC events in the $t\bar{t}\gamma$-CR as functions of N_{jets} and $p_{\text{T}}^{\gamma}/\sqrt{H_{\text{T}}}$. The Z + jets estimate is obtained using the same method as previously described in Section 6.1, but using $e\mu\gamma$ events instead of $ee\gamma/\mu\mu\gamma$ events. The correlation factor is fixed to $R = 1.30 \pm 0.04(\text{stat.})$ (see Section 6.1). Another background also present in this region is from diboson events where one lepton is misidentified as a photon ($WZ \to \ell\nu\ell\ell$). A 30% uncertainty is assigned to this background, which accounts for uncertainties in the inclusive cross-sections due to possible higher-order contributions. Good agreement is seen between data and MC events in the $t\bar{t}\gamma$-CR. The largest discrepancy can be seen in the 0-jet bin. Such mismodelling has negligible impact on the analysis since the contribution of $t\bar{t}\gamma$ and diboson processes for events with no jets in the SR is more than one order of magnitude smaller than the signal.

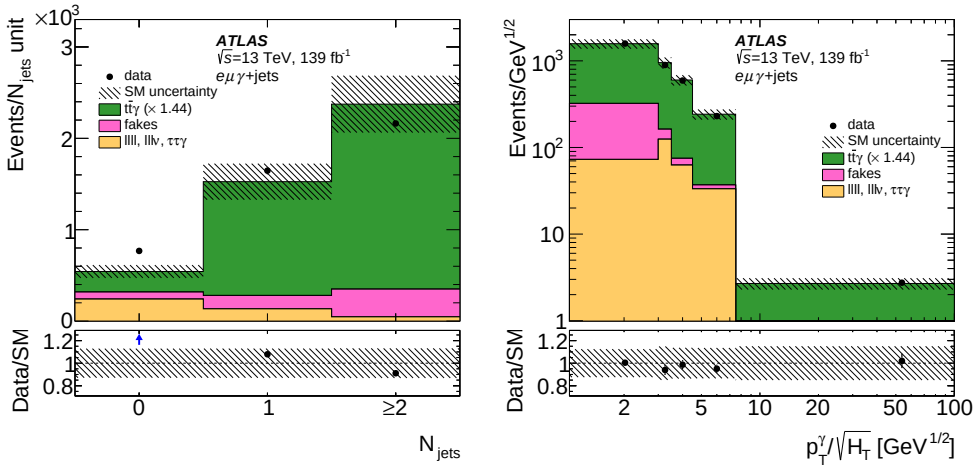

(a) (b)

Figure 2: Data (black dots) in the $t\bar{t}\gamma$-CR compared with scaled simulated $t\bar{t}\gamma$ events, simulated diboson events and fake photons estimated with a sideband method. The bottom panel shows the ratio of observed data events to the sum of the estimates. The simulated signal and background distributions are stacked to produce the figures. The hatched band represents the statistical and systematic uncertainties of the SM background yields added in quadrature.

The other backgrounds (tribosons and dibosons) contribute around 1% of the total expected yield in the SR. For this reason they are estimated directly from MC simulation. Other even smaller backgrounds (such as $H \to Z\gamma$) are neglected, since they contribute less than 0.03% of the events in total.

6.4 Data event yield, signal, and background estimate comparisons in the signal region

Table 3 shows the data event yield and the signal and background estimates in the SR. The Sherpa 2.2.11 MC sample is used for the $Z\gamma$+jets process. Table 3 includes the statistical uncertainties, experimental uncertainties (see Section 8), and background systematic uncertainties (as described in Section 6).

Table 3: Data yield and the signal and background estimates in the SR. The systematic uncertainty includes experimental uncertainties and background uncertainties.

Source	$ee + \mu\mu$
$Z\gamma$+jets signal	73 500 ± 50 (stat.) ± 2 600 (syst.)
Z + jets	9 800 ± 460 (stat.) ± 2 100 (syst.)
$t\bar{t}\gamma$	3 600 ± 10 (stat.) ± 540 (syst.)
Pile-up	2 500 ± 70 (stat.) ± 700 (syst.)
Multiboson	950 ± 5 (stat.) ± 280 (syst.)
$tW\gamma$	150 ± 1 (stat.) ± 45 (syst.)
Total prediction	90 500 ± 500 (stat.) ± 3 500 (syst.)
Data	96 410

Figures 3 and 4 show a comparison between the data and the expected SM events in a subset of distributions. The Sherpa 2.2.11 signal sample is scaled by a normalisation factor of 1.08 to match the rate in the data. The normalisation factor is obtained from the ratio of the measured yields to the predicted yields from Sherpa 2.2.11, as shown in Table 3. The hatched band in the figures shows the impact of the systematic uncertainties, as also shown in Table 3. In general, good agreement is observed between the data and the SM estimates. Observables inclusive in the number of jets are well modelled; in some bins of some observables, small differences are observed which, when comparing the measured differential cross sections with the predictions, are covered by the theoretical uncertainties (see Section 9).

7 Cross-section determination

7.1 Fiducial region at particle level

The measurements are unfolded to a fiducial phase space defined by particle-level quantities. The fiducial phase space in this analysis is built to be as close as possible to the detector-level selection discussed in Section 4, with selection criteria that minimise the extrapolation and allow comparisons with theoretical predictions. The phase space is selected for $Z\gamma \to \ell^+\ell^-\gamma$ events, with ℓ being either an electron or muon. Only stable particles (with a mean lifetime $c\tau > 10$ mm) are used in the definition of the fiducial region. Additionally, only 'prompt' leptons (dressed) and photons (only those that do not originate from hadron decays) are considered.

Leptons are required to pass the same p_{T} requirements as in the SR: $p_{\mathrm{T}}(\ell_1) > 30$ GeV, $p_{\mathrm{T}}(\ell_2) > 25$ GeV. However, the η requirements are different: for both electrons and muons $|\eta(\ell)| < 2.47$ is required, since at particle level the discontinuities in the detector are not present. A particle-level isolation requirement is applied to photons: the scalar sum of the E_{T} of all particles, except muons and neutrinos, within a cone of size $\Delta R = 0.2$ around the photon must be less than 7% of the transverse energy of the photon, E_{T}^{γ}. This selection is the same as in Ref. [14] and is optimised to achieve the same level of acceptance in both the detector-level and particle-level selections. Photons are rejected if they are within $\Delta R = 0.4$ of any lepton. Jets are obtained by clustering stable particles, excluding prompt leptons and using the anti-k_t algorithm with a radius parameter of $R = 0.4$. Photons within a cone of size $\Delta R = 0.1$ around prompt leptons are also excluded. Jets are defined in the same way as for the SR, by requiring $p_{\mathrm{T}} > 30$ GeV for $|\eta| < 2.5$ and $p_{\mathrm{T}} > 50$ GeV for $2.5 < |\eta| < 4.5$. Jets are rejected if they are within $\Delta R = 0.4$ of any photon. As

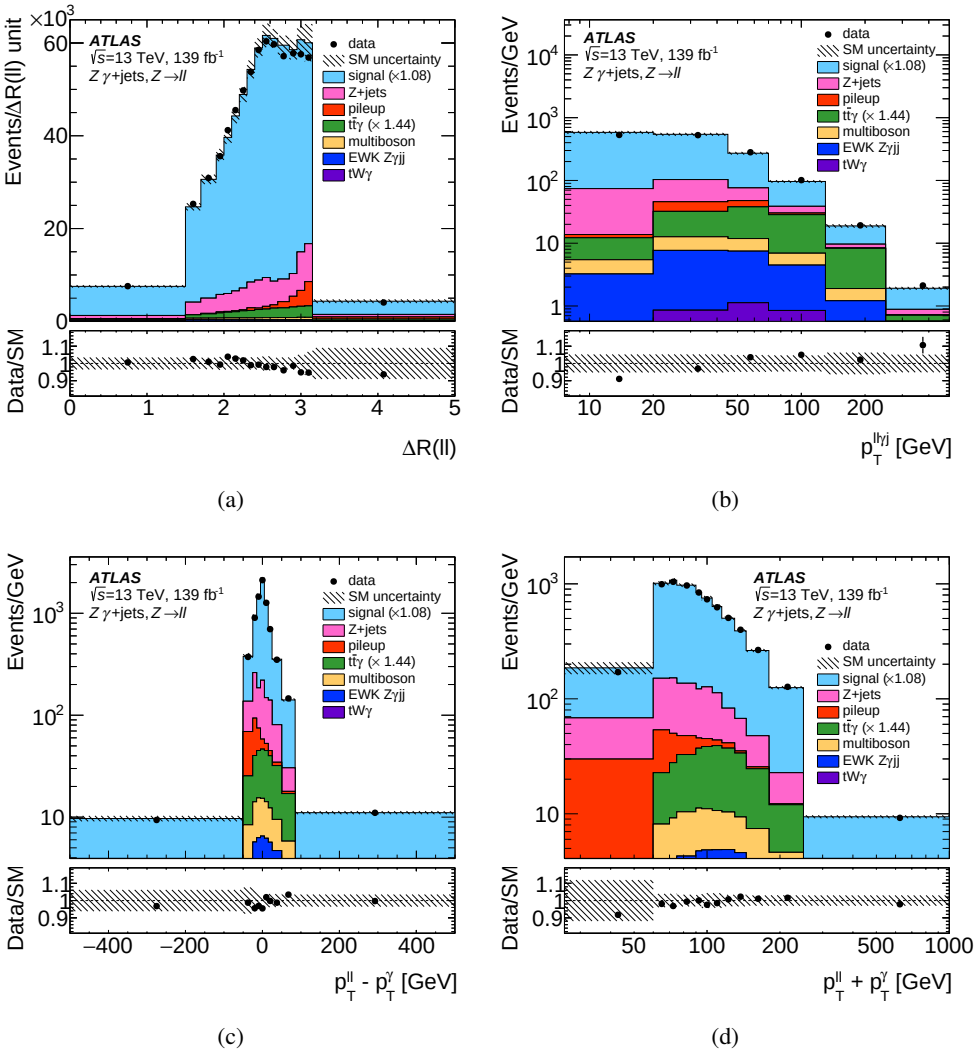

Figure 3: The measured (a) $\Delta R(\ell,\ell)$, (b) $p_{\mathrm{T}}^{\ell\ell\gamma\mathrm{j}}$, (c) $p_{\mathrm{T}}^{\ell\ell} - p_{\mathrm{T}}^{\gamma}$, and (d) $p_{\mathrm{T}}^{\ell\ell} + p_{\mathrm{T}}^{\gamma}$ distribution (dots) in the signal region. The error bars represent the data statistical uncertainty; for most of the points, the error bars are smaller than the marker size and, thus, not visible. The MC simulation of the signal from Sherpa 2.2.11 (blue histograms) and various backgrounds are also included. The signal and background distributions are stacked to produce the figures. The variable bin width is taken into account in the vertical scale. The lower part of each figure shows the ratio of the data to the expected total SM distribution. The hatched band represents the statistical and systematic uncertainties of the SM background yields added in quadrature, excluding theory uncertainties of the signal.

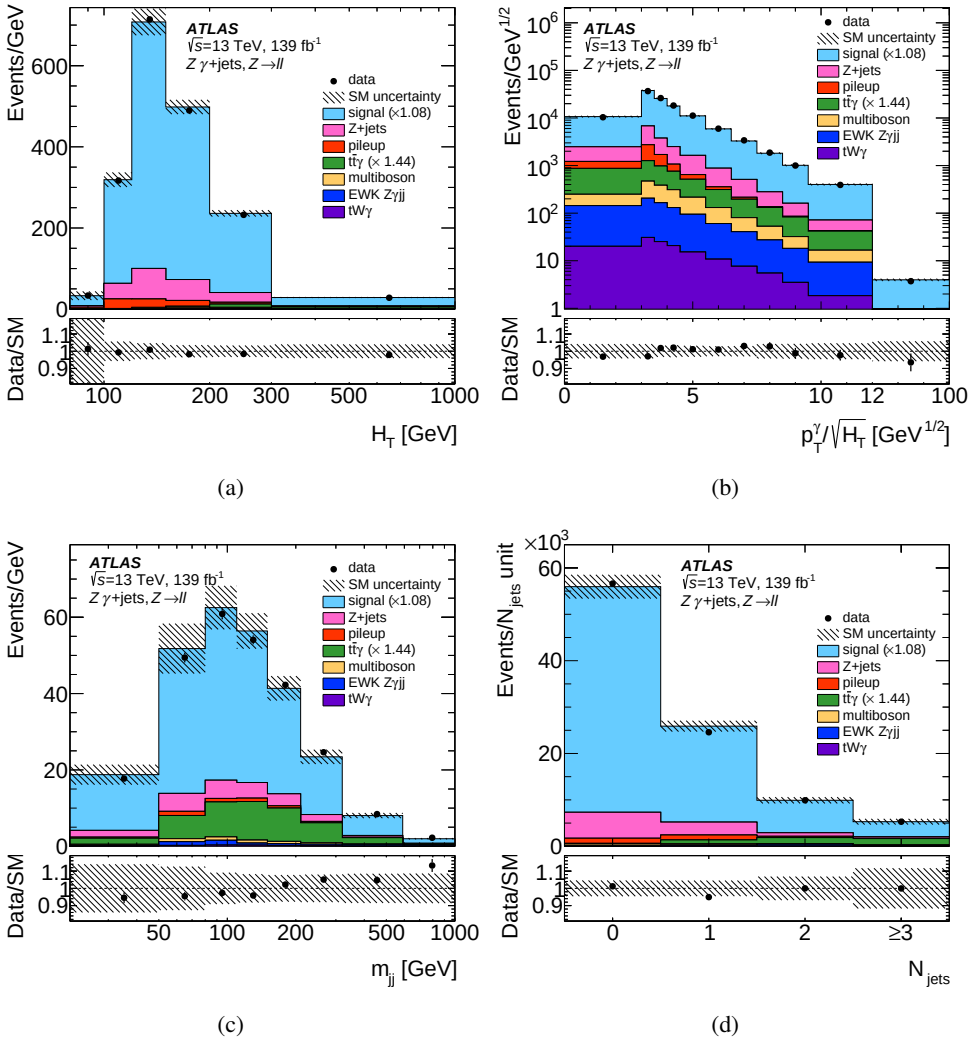

Figure 4: The measured (a) H_{T}, (b) $p_{\mathrm{T}}^{\gamma}/\sqrt{H_{\mathrm{T}}}$, (c) m_{jj}, and (d) N_{jets} distribution (dots) in the signal region. The error bars represent the data statistical uncertainty; for most of the points, the error bars are smaller than the marker size and, thus, not visible. The MC simulation of the signal from SHERPA 2.2.11 (blue histograms) and various backgrounds are also included. The signal and background distributions are stacked to produce the figures. The variable bin width is taken into account in the vertical scale. The lower part of each figure shows the ratio of the data to the expected total SM distribution. The hatched band represents the statistical and systematic uncertainties on the SM background yields added in quadrature, excluding theory uncertainties of the signal.

in the SR, $m_{\ell\ell} > 40$ GeV and $m_{\ell\ell} + m_{\ell\ell\gamma} > 182$ GeV requirements are applied. A pair of opposite-sign, same-flavour leptons is selected, and no additional veto on the number of leptons is applied. Table 4 summarises the fiducial selection used in the analysis.

Table 4: Definition of the fiducial region at particle level.

Quantity	Selection criteria
Lepton kinematics	$p_{\mathrm{T}}(\ell_1) > 30$ GeV, $p_{\mathrm{T}}(\ell_2) > 25$ GeV, $\lvert\eta\rvert < 2.47$
Photon kinematics	$p_{\mathrm{T}} > 30$ GeV, $\lvert\eta\rvert < 2.37$, $\Delta R(\gamma, \ell) > 0.4$
Photon isolation	$E_{\mathrm{T}}^{\mathrm{iso}}/E_{\mathrm{T}}^{\gamma} < 0.07$
Jet kinematics	($p_{\mathrm{T}} > 30$ GeV if $\lvert\eta\rvert < 2.5$) or ($p_{\mathrm{T}} > 50$ GeV if $2.5 < \lvert\eta\rvert < 4.5$), $\Delta R(\gamma, \mathrm{jet}) > 0.4$
Invariant mass	$m_{\ell\ell} > 40$ GeV, $m_{\ell\ell} + m_{\ell\ell\gamma} > 182$ GeV

7.2 Fiducial and differential cross section

The fiducial cross section is evaluated in the fiducial region described in the previous subsection. It is obtained with the following formula:

$$\sigma^{\mathrm{fid}} = \frac{N_{\mathrm{obs}} - N_{\mathrm{bkg}}}{C \times \mathcal{L}},$$

where N_{obs} and N_{bkg} are the observed number of events and the expected number of background events, respectively, $\mathcal{L}$ is the integrated luminosity, and C is the correction factor which accounts for detector inefficiency and resolution effects. The factor C is calculated as the number of simulated $Z\gamma$+jets events entering the detector-level SR divided by the number of simulated $Z\gamma$+jets events entering the fiducial volume. The inclusive C factor is obtained with Sherpa 2.2.11 MC samples, combining the ee and $\mu\mu$ channels; its value is found to be $C = 0.543 \pm 0.001$ (stat) ± 0.02 (syst).

Differential cross sections are evaluated in the fiducial signal region for several observables. The event yields in the e^+e^- and $\mu^+\mu^-$ decay channels are added together and unfolded in a single step. The distributions are unfolded using an iterative Bayesian method [81], with two iterations as the nominal number. The $Z\gamma$+jets events simulated with Sherpa 2.2.11 are used to produce the response matrices needed to correct for the migration between bins in the detector- and particle-level distributions. These migrations are mainly due to the jet reconstruction. Additionally, the unfolding corrects for fiducial and reconstruction efficiencies. These are respectively the probability of having particle-level events satisfy the detector-level SR criteria, and the probability that detector-level events originate from outside the fiducial region.

8 Systematic uncertainties

Systematic uncertainties from several different sources affect this measurement: experimental uncertainties due to detector reconstruction, uncertainties in the background estimate (from simulated samples as well as data-driven methods, as described in Section 6), systematic uncertainties in the unfolding, and theoretical

uncertainties in the signal prediction. The individual sources of uncertainty are varied by $\pm 1\sigma$ in the MC simulations and propagated through the analysis separately. The uncertainties are propagated to the cross sections by modifying the migration matrix and computing the resulting deviation from the nominal cross section. This deviation is taken as the systematic uncertainty.

Experimental uncertainties account for the finite resolution of the objects reconstructed by the ATLAS detector, their calibration, and the modelling of the reconstruction in the simulation. Uncertainties affecting the electrons and photons include the uncertainties in the energy scale and resolution [66], while for muons, uncertainties are considered for the momentum resolution [67]. Both leptons and photons have uncertainties in the efficiency of the identification and the isolation [66, 67]. Uncertainties in the lepton trigger efficiencies are also considered [64, 65]. Jet uncertainties account for both the energy scale (JES) and the resolution (JER) [82]. The JES uncertainties take into account detector modelling, statistical effects, flavour composition, and the description of pile-up jets. The JVT efficiency uncertainties are also considered [74]. Additional uncertainties are added to take into account the modelling of the number of pp collisions. An uncertainty of 1.7% in the total integrated luminosity is considered in this analysis.

The statistical uncertainty in the measured cross sections is evaluated using 'toy experiments' (bootstrap technique [83]). Statistically-independent replicas of the data distributions are used and each one of them is then unfolded; the root mean square (RMS) of the replicas distribution is used as the uncertainty. For the MC samples, the limited number of simulated events mainly affects the estimation of the migration matrices. This statistical uncertainty is also calculated using toy experiments and found to be small.

The unfolding procedure is based on an assumption, namely our choice of a simulated signal sample. This choice can bias the results, and a systematic uncertainty to account for this effect is obtained through a data-driven closure test. The simulated signal distributions are reweighted with a smooth function obtained by requiring that the detector-level distribution matches the data (after background subtraction). The reweighted distribution is then unfolded, treating this sample as pseudo-data, and using the migration matrix from the reweighted distributions. The uncertainty is obtained by comparing this result with the nominal unfolded result.

Systematic uncertainties in the cross sections due to the theoretical modelling are obtained by unfolding the data with a migration matrix calculated using alternative signal simulations. Uncertainties in the signal predictions are due to missing higher-order contributions in the cross-section calculation, the uncertainties from the PDF choice, and the uncertainties in α_s. The effect of QCD scale uncertainties is estimated by halving and doubling the renormalisation and factorisation scales in the signal simulation relative to their nominal values. Uncertainties are obtained by taking an envelope: in each bin the largest resulting change is used as the uncertainty. Additional uncertainties are added to account for the choice of a specific PDF in the cross-section calculation. Following the PDF4LHC recommendation [84], the NNPDF3.0NNLO_as_0118 PDF set is used as the nominal set, and is compared with results obtained with weights stored in the SHERPA samples. An envelope is then taken of all the variations. A similar approach is used for the α_s variations, where the NNPDF3.0NNLO_as_0117 and NNPDF3.0NNLO_as_0119 PDF sets are used. For the theory predictions, uncertainties are obtained by taking an envelope of the difference between the nominal unfolded results and their variations.

Uncertainties for the background estimates are taken to be 30% in the diboson cross section and 15% in the $t\bar{t}\gamma$ cross section (which corresponds to the uncertainty in the normalisation factor from the LO cross section to the NLO cross section [51]). The uncertainty of 30% in the diboson cross section covers both the nominal uncertainty [85] and the typical size of the mismodelling of non-prompt objects. The systematic

Table 5: Impact of the different systematic uncertainties on the measured $Z\gamma$+jets cross section as a function of N_{jets} in each bin of the distribution.

N_{jets}	0	1	2	> 2
Source	Uncertainty [%]			
Electrons	1.0	0.9	0.8	0.8
Muons	0.3	0.3	0.3	0.4
Jets	1.7	1.7	4.5	8.8
Photons	1.4	1.3	1.3	1.2
Pile-up	2.1	0.8	0.2	0.3
Background	1.8	1.8	3.0	4.4
MC statistical	0.1	0.2	0.3	0.4
Data statistical	0.8	1.5	1.8	1.9
Luminosity	1.7	1.7	1.7	1.7
Theory	0.6	0.2	1.4	1.0
Total	4.2	3.8	6.3	10.3

uncertainties for the Z + jets background are estimated as described in Section 6.1 and propagated through the unfolding framework.

Table 5 shows the breakdown of the systematic uncertainties in the cross section as a function of N_{jets}. The last row in the table is the total relative uncertainty obtained as the sum in quadrature of each systematic uncertainty and statistical uncertainty. The increase in jet systematic uncertainties with the number of jets, is due to the modelling of pile-up jets, forward jet modelling, and statistical fluctuations.

9 Results

The measured fiducial cross section for $Z\gamma$ production is $\sigma = 533.7 \pm 2.1(\text{stat}) \pm 12.4(\text{syst}) \pm 9.1(\text{lumi})$ fb, as presented in Ref. [14]. The predicted fiducial cross sections are $479.5 \pm 0.3(\text{stat})$ fb from Sherpa 2.2.11 interfaced with MEPS@LO and $493.0 \pm 3.0(\text{stat})$ fb from MiNNLO$_{\text{PS}}$.

The measured differential cross sections as functions of the different observables are shown in Figures 5 to 12. To obtain these results the unfolding uses as signal the $Z\gamma$+jets MC samples added together with the MC sample for purely electroweak production of $Z\gamma jj$. The theoretical predictions from Sherpa 2.2.4, Sherpa 2.2.11 (both interfaced with MEPS@LO and using the NNPDF3.0nnlo PDF set) and MadGraph5_aMC@NLO (interfaced with Pythia 8.212 and using the NNPDF3.0nlo PDF set), and the NNLO predictions from MiNNLO$_{\text{PS}}$ (using the NNPDF3.0nnlo PDF set) and MATRIX (using the CT14nnlo PDF set) are compared with the measurements in these figures. The purely electroweak production of $Z\gamma jj$ has not been added to the theoretical predictions shown in these figures; this contribution is estimated to be around 1%. In general, Sherpa samples underestimate the total cross section, with Sherpa 2.2.11 (NLO) being higher than Sherpa 2.2.4, while MadGraph5_aMC@NLO, MiNNLO$_{\text{PS}}$ and MATRIX show generally good agreement for the total cross section. Between the two Sherpa samples, Sherpa 2.2.11 also shows generally better agreement in the distribution shapes, especially for the number of jets.

The Z boson momentum is a fundamental observable, correlated with the jet activity, and its difference from p_{T}^{γ} is an observable that probes pQCD over a wide range of scales, while $p_{\mathrm{T}}^{\ell\ell} + p_{\mathrm{T}}^{\gamma}$ describes the hard scale of the process. Figure 5 shows the differential cross sections as functions of the observables $p_{\mathrm{T}}^{\ell\ell}$, $p_{\mathrm{T}}^{\ell\ell} - p_{\mathrm{T}}^{\gamma}$, $p_{\mathrm{T}}^{\ell\ell} + p_{\mathrm{T}}^{\gamma}$, and $\Delta R(\ell, \ell)$. All the predictions show good agreement with the measurements, although Sherpa generally underestimates the data. The MATRIX calculations are also in good agreement with the measurements.

Jet multiplicity is a fundamental observable to probe QCD and additional soft radiation [24]. The ratio $p_{\mathrm{T}}^{\mathrm{jet2}}/p_{\mathrm{T}}^{\mathrm{jet1}}$ in particular is an observable that tests the limits of PS effects and resummation of Sudakov logarithms. Differential cross sections for jet observables are shown in Figure 6. The differential cross section is dominated by events with zero jets, and rapidly falls off with increasing QCD emission. The leading and subleading jets are mostly produced with similar p_{T}; however, the cross section is not zero at $p_{\mathrm{T}}^{\mathrm{jet2}}/p_{\mathrm{T}}^{\mathrm{jet1}} = 0.1$, which means that the subleading jet has only 10% of the p_{T} of the leading jet. In general, the MC samples are in good agreement with the data; however, at high jet multiplicity and high jet transverse momentum Sherpa 2.2.4 predicts higher yields than Sherpa 2.2.11, while MadGraph5_aMC@NLO has lower yields in N_{jets} but it is comparable to the Sherpa samples in the leading ($p_{\mathrm{T}}^{\mathrm{jet1}}$) and subleading ($p_{\mathrm{T}}^{\mathrm{jet2}}$) jet momenta. The MiNNLO$_{\mathrm{PS}}$ calculation instead predicts softer jets and lower jet multiplicity, while the MATRIX prediction models the jet momentum spectrum better, but predicts higher jet multiplicity. It is worth noting that MATRIX produces no more than two jets, so the last bin is empty for this calculation. The ratio $p_{\mathrm{T}}^{\mathrm{jet2}}/p_{\mathrm{T}}^{\mathrm{jet1}}$ is equally well described by both Sherpa models and MadGraph5_aMC@NLO. The MATRIX prediction is also in good agreement, while MiNNLO$_{\mathrm{PS}}$ underestimates the data.

The invariant mass of the two leading jets is an important observable that describes the hard scale of the process, and its precise modelling is fundamental for the $Z\gamma jj$ QCD background in measurements of purely electroweak $Z\gamma jj$ production or searches for new physics [86]. The m_{jj} distribution in Figure 7 is well modelled in general, except for MiNNLO$_{\mathrm{PS}}$, which underestimates the highest bins. The MATRIX prediction shows good agreement, except for a few bins with some overestimations between 60 and 100 GeV. The invariant mass $m_{\ell\ell\gamma j}$ is a variable sensitive to the hard scale of the process, and is also well modelled by the predictions, except for the last bins in the case of MiNNLO$_{\mathrm{PS}}$, where an underestimation is observed. The MATRIX prediction also shows good agreement, with a small overestimation (within uncertainties) in the last bins.

Figure 8 shows additional jet observables H_{T}, $p_{\mathrm{T}}^{\gamma}/\sqrt{H_{\mathrm{T}}}$, $\Delta\phi(\mathrm{jet}, \gamma)$, and $p_{\mathrm{T}}^{\ell\ell\gamma\mathrm{j}}$. The H_{T} and $p_{\mathrm{T}}^{\gamma}/\sqrt{H_{\mathrm{T}}}$ observables are both well described by Sherpa 2.2.4 and Sherpa 2.2.11, while MadGraph5_aMC@NLO, MATRIX, and MiNNLO$_{\mathrm{PS}}$ underestimate the last bin of H_{T}. The $\Delta\phi(\mathrm{jet}, \gamma)$ distribution is important for PS corrections in QCD predictions in phase-space regions with soft QCD emission [24]. The measurement shows a preference for events in which the photon and the leading jet are back-to-back. The $\Delta\phi(\mathrm{jet}, \gamma)$ observable is well modelled by all the predictions, except in the very first bin of the MATRIX prediction. The $p_{\mathrm{T}}^{\ell\ell\gamma\mathrm{j}}$ observable is well modelled within uncertainties by both Sherpa samples and MadGraph5_aMC@NLO, whereas the MiNNLO$_{\mathrm{PS}}$ and MATRIX predictions show some deviation from the data distributions.

Figure 9 shows the cross sections as functions of $\cos\theta_{\mathrm{CS}}$ and ϕ_{CS}, which are sensitive to the polarisation of the Z boson. The variation of $\cos\theta_{\mathrm{CS}}$ with $p_{\mathrm{T}}^{\ell\ell}$ is mainly due to the lepton selection, which translates into differences in acceptance in each $p_{\mathrm{T}}^{\ell\ell}$ region. For these variables, the Sherpa, MadGraph5_aMC@NLO and MiNNLO$_{\mathrm{PS}}$ predictions are in general in good agreement for the shapes, although, as already mentioned, Sherpa 2.2.4 and 2.2.11 generally underestimate the data. The MATRIX predictions show some small disagreement in $\cos\theta_{\mathrm{CS}}$ in the very first $p_{\mathrm{T}}^{\ell\ell}$ bin, but otherwise show very good agreement.

The ratio $p_{\mathrm{T}}^{\ell\ell\gamma}/m_{\ell\ell\gamma}$ is an important resolution variable for probing the effects of Sudakov-logarithm terms in different regimes of the hard scale of the process. The ratio $p_{\mathrm{T}}^{\ell\ell\gamma}/m_{\ell\ell\gamma}$ in all the $m_{\ell\ell\gamma}$ slices is presented in Figure 10. These observables are better modelled by Sherpa 2.2.11 than by Sherpa 2.2.4. The MiNNLO$_{\mathrm{PS}}$ prediction shows good agreement in all the $m_{\ell\ell\gamma}$ slices, while MATRIX overestimates the data in the lowest bin in $p_{\mathrm{T}}^{\ell\ell\gamma}/m_{\ell\ell\gamma}$.

The $p_{\mathrm{T}}^{\ell\ell} - p_{\mathrm{T}}^{\gamma}$ and $p_{\mathrm{T}}^{\ell\ell\gamma\mathrm{j}}$ distributions offer an important probe of additional soft QCD emissions, in increasing hard scale of the process, described by $p_{\mathrm{T}}^{\ell\ell} + p_{\mathrm{T}}^{\gamma}$ and $p_{\mathrm{T}}^{\ell\ell\gamma}$, respectively. The $p_{\mathrm{T}}^{\ell\ell} - p_{\mathrm{T}}^{\gamma}$ distributions become more asymmetric in regimes with a harder scale of the process. All the distributions as function of $p_{\mathrm{T}}^{\ell\ell} - p_{\mathrm{T}}^{\gamma}$ in different regions of $p_{\mathrm{T}}^{\ell\ell} + p_{\mathrm{T}}^{\gamma}$ (Figure 11) are well modelled by all the MC models and the MATRIX predictions, except for the last two bins in the region with $p_{\mathrm{T}}^{\ell\ell} + p_{\mathrm{T}}^{\gamma} > 300$ GeV, where MadGraph5_aMC@NLO slightly overestimates the data. The $p_{\mathrm{T}}^{\ell\ell\gamma\mathrm{j}}$ distributions in different regions of $p_{\mathrm{T}}^{\ell\ell\gamma}$ (Figure 12) are well modelled by Sherpa and MadGraph5_aMC@NLO, while the MiNNLO$_{\mathrm{PS}}$ predictions underestimate the data for $p_{\mathrm{T}}^{\ell\ell\gamma} > 75$ GeV. The MATRIX prediction exhibits a softer spectrum than the other predictions.

In summary, the Sherpa and MadGraph5_aMC@NLO predictions describe the data well, especially for observables involving jets, although Sherpa underestimates the measured total cross section. The MiNNLO$_{\mathrm{PS}}$ and MATRIX predictions give an adequate description of the measurements, but some deviations from the data are observed at high jet multiplicity.

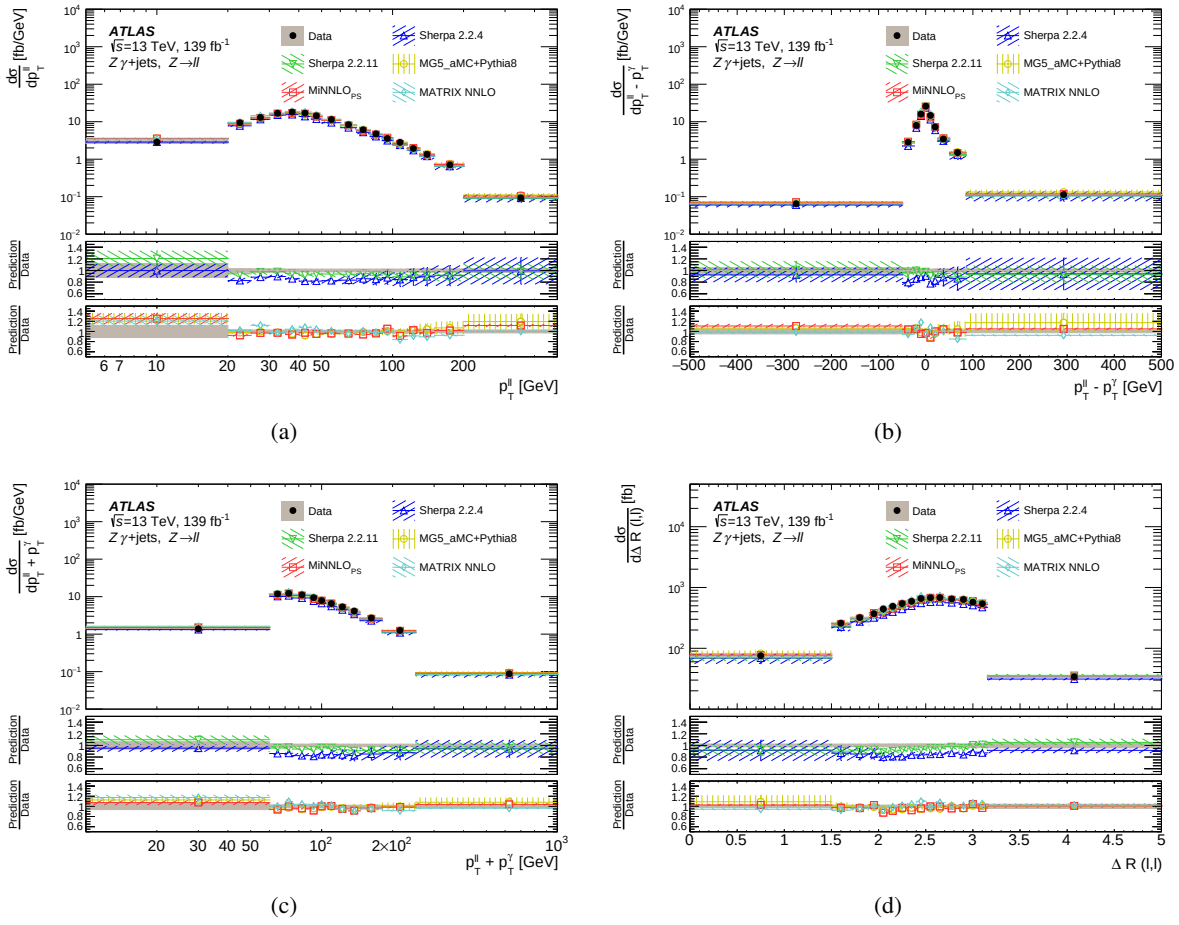

Figure 5: Measured differential cross section (black data points) as a function of the observables (a) $p_{\mathrm{T}}^{\ell\ell}$, (b) $p_{\mathrm{T}}^{\ell\ell} - p_{\mathrm{T}}^{\gamma}$, (c) $p_{\mathrm{T}}^{\ell\ell} + p_{\mathrm{T}}^{\gamma}$, and (d) $\Delta R(\ell, \ell)$. Error bands on the data points show the statistical uncertainty, while the grey area shows the total uncertainty in the unfolded result. Measured cross sections are compared with SM predictions from event generators at particle level: Sherpa 2.2.4, Sherpa 2.2.11, MadGraph5_aMC@NLO+Pythia 8 (MG5_aMC+Pythia8 in the legend), and MiNNLO$_{\mathrm{PS}}$. Fixed-order calculation results from MATRIX NNLO are also shown. Dashed bands represent the statistical uncertainty and theoretical uncertainty (PDF and scale variations). The bottom panels show the ratio of the SM prediction to the measured cross section.

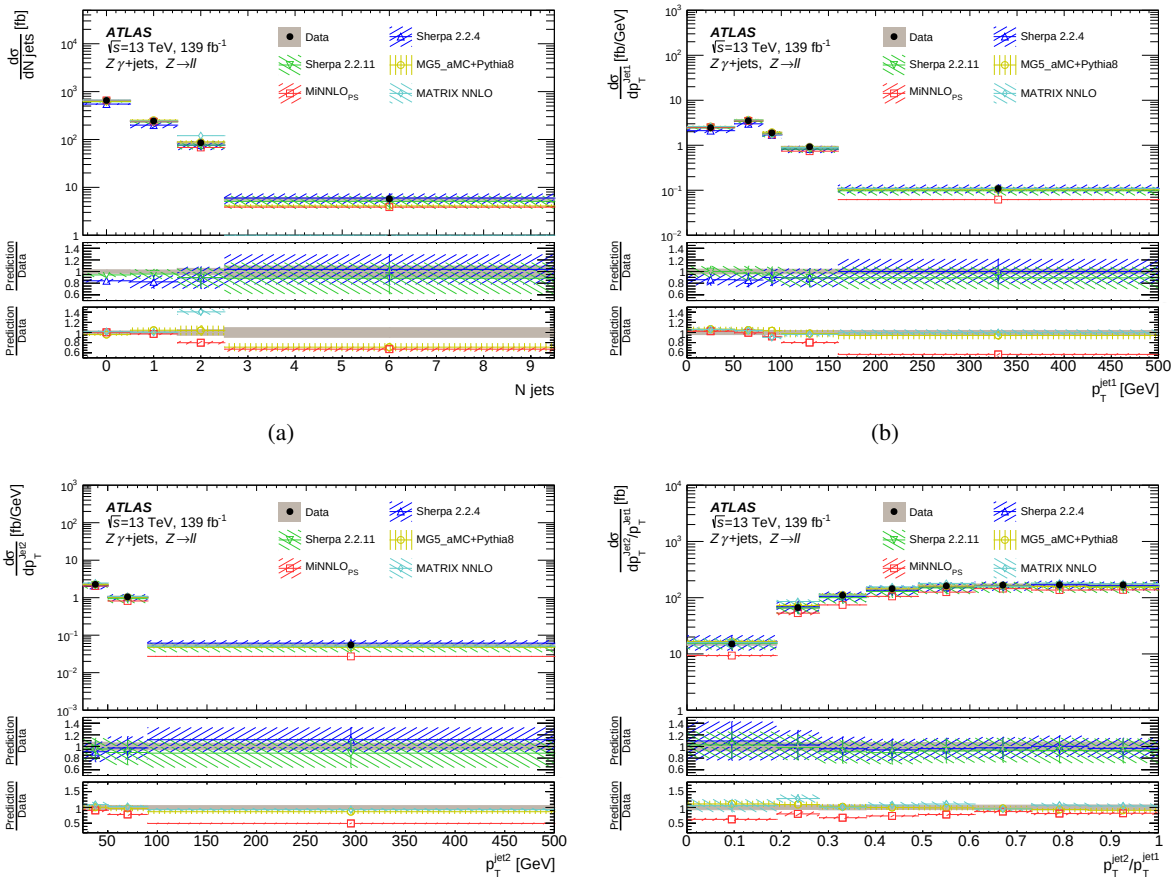

Figure 6: Measured differential cross section (black data points) as a function of the observables (a) N_{jets}, (b) $p_{\text{T}}^{\text{jet1}}$, (c) $p_{\text{T}}^{\text{jet2}}$, and (d) $p_{\text{T}}^{\text{jet2}}/p_{\text{T}}^{\text{jet1}}$. Error bands on the data points show the statistical uncertainty, while the grey area shows the total uncertainty in the unfolded result. Measured cross sections are compared with SM predictions from event generators at particle level: Sherpa 2.2.4, Sherpa 2.2.11, MadGraph5_aMC@NLO+Pythia 8 (MG5_aMC+Pythia8 in the legend), and MiNNLO$_{\text{PS}}$. Fixed-order calculation results from MATRIX NNLO are also shown. Dashed bands represent the statistical uncertainty and theoretical uncertainty (PDF and scale variations). The bottom panels show the ratio of the SM prediction to the measured cross section.

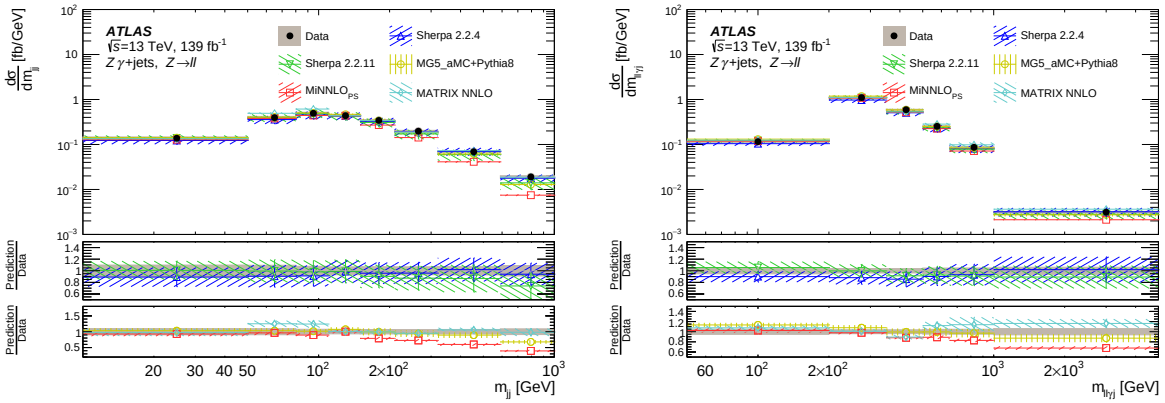

(a) (b)

Figure 7: Measured differential cross section (black data points) as a function of the observables (a) m_{jj} and (b) $m_{\ell\ell\gamma j}$. Error bands on the data points show the statistical uncertainty, while the grey area shows the total uncertainty in the unfolded result. Measured cross sections are compared with SM predictions from event generators at particle level: SHERPA 2.2.4, SHERPA 2.2.11, MADGRAPH5_AMC@NLO+PYTHIA 8 (MG5_aMC+Pythia8 in the legend), and MiNNLO$_{\text{PS}}$. Fixed-order calculation results from MATRIX NNLO are also shown. Dashed bands represent the statistical uncertainty and theoretical uncertainty (PDF and scale variations). The bottom panels show the ratio of the SM prediction to the measured cross section.

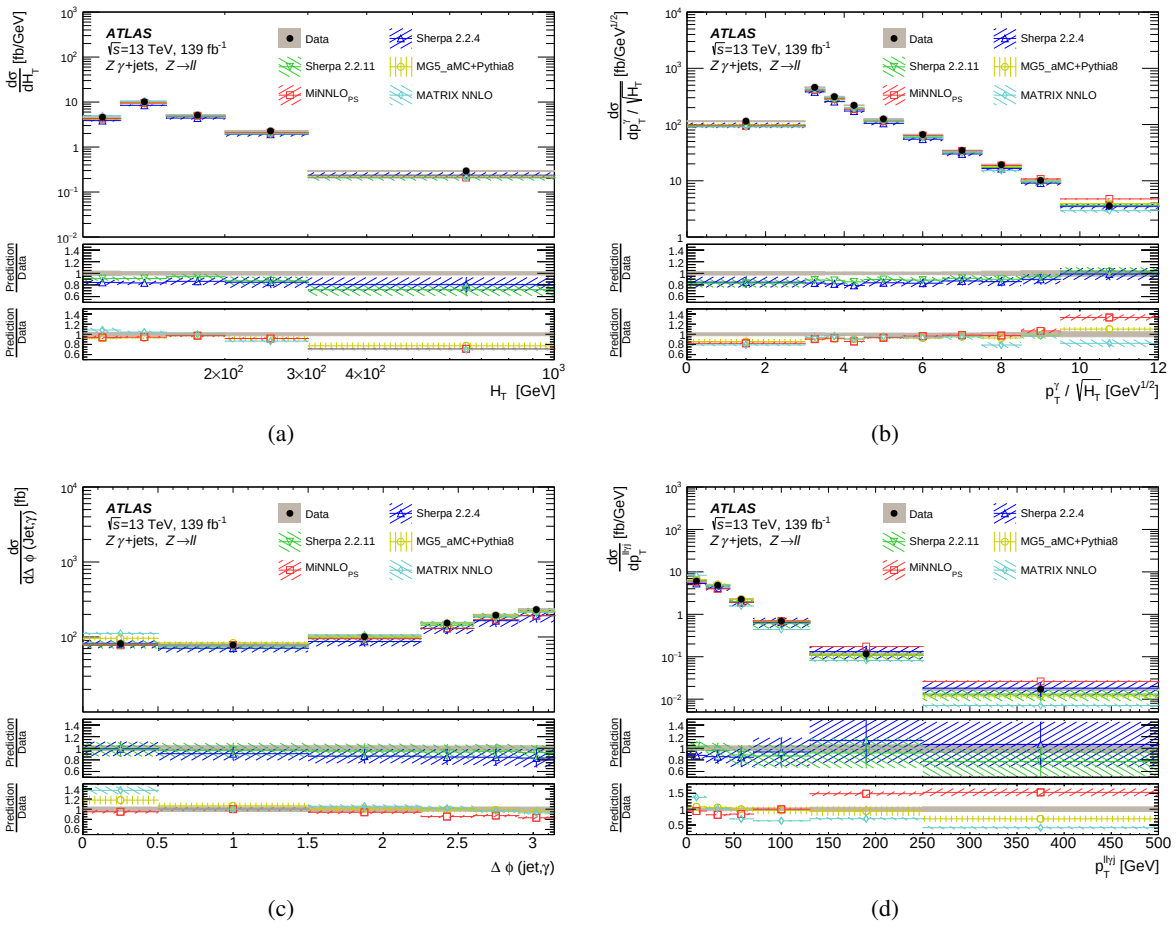

Figure 8: Measured differential cross section (black data points) as a function of the observables (a) H_{T}, (b) $p_{\mathrm{T}}^{\gamma}/\sqrt{H_{\mathrm{T}}}$, (c) $\Delta\phi(\mathrm{jet},\gamma)$, and (d) $p_{\mathrm{T}}^{\ell\ell\gamma\mathrm{j}}$. Error bands on the data points show the statistical uncertainty, while the grey area shows the total uncertainty in the unfolded result. Measured cross sections are compared with SM predictions from event generators at particle level: Sherpa 2.2.4, Sherpa 2.2.11, MadGraph5_aMC@NLO+Pythia 8 (MG5_aMC+Pythia8 in the legend), and MiNNLO$_{\mathrm{PS}}$. Fixed-order calculation results from MATRIX NNLO are also shown. Dashed bands represent the statistical uncertainty and theoretical uncertainty (PDF and scale variations). The bottom panels show the ratio of the SM prediction to the measured cross section.

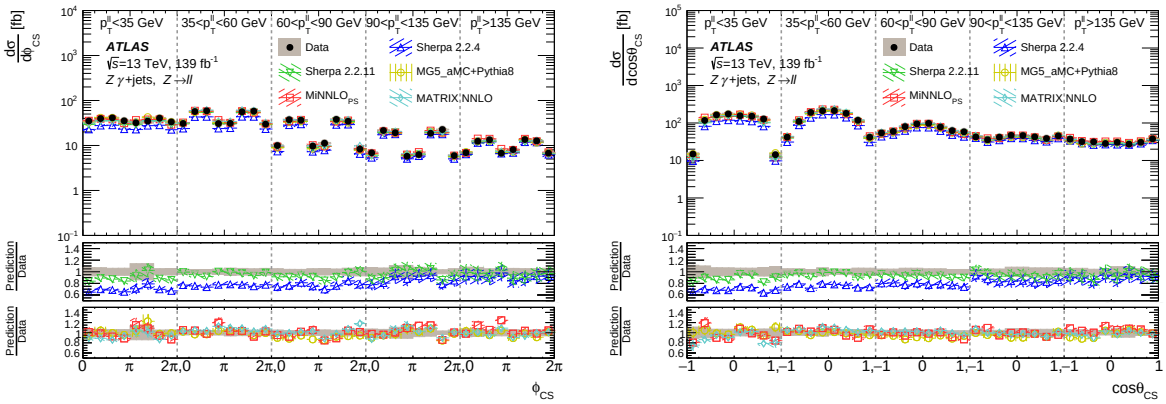

(a) (b)

Figure 9: Measured differential cross section (black data points) as a function of the observables (a) ϕ_{CS} and (b) $\cos\theta_{\mathrm{CS}}$, in different bins of $p_{\mathrm{T}}^{\ell\ell}$. Error bands on the data points show the statistical uncertainty, while the grey area shows the total uncertainty in the unfolded result. Measured cross sections are compared with SM predictions from event generators at particle level: Sherpa 2.2.4, Sherpa 2.2.11, MadGraph5_aMC@NLO+Pythia 8 (MG5_aMC+Pythia8 in the legend), and MiNNLO$_{\mathrm{PS}}$. Fixed-order calculation results from MATRIX NNLO are also shown. Dashed bands represent the statistical uncertainty and theoretical uncertainty (PDF and scale variations). The bottom panels show the ratio of the SM prediction to the measured cross section.

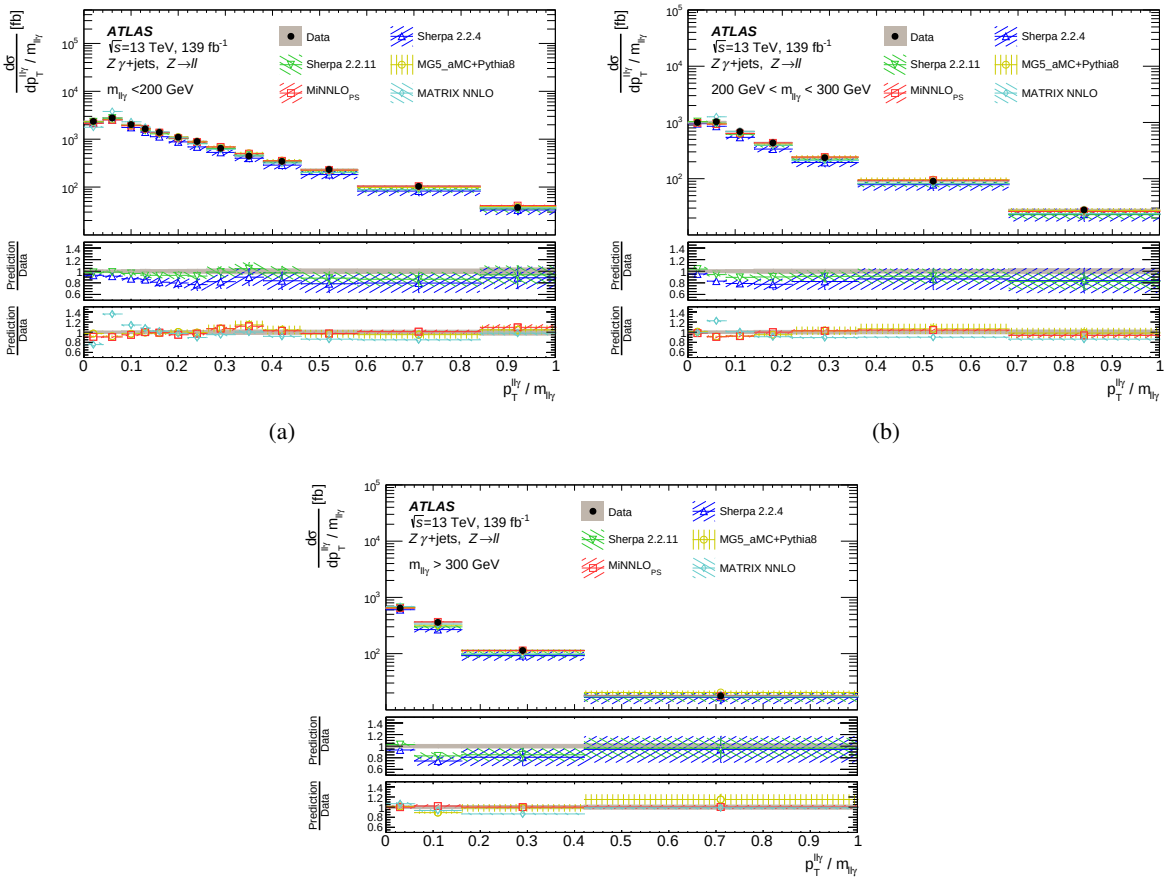

(a) (b)

(c)

Figure 10: Measured differential cross section (black data points) as a function of $p_{\mathrm{T}}^{\ell\ell\gamma}/m_{\ell\ell\gamma}$ (a) in $m_{\ell\ell\gamma} < 200$ GeV, (b) in 200 GeV $< m_{\ell\ell\gamma} <$ 300 GeV, and (c) in $m_{\ell\ell\gamma} > 300$ GeV. Error bands on the data points show the statistical uncertainty, while the grey area shows the total uncertainty in the unfolded result. Measured cross sections are compared with SM predictions from event generators at particle level: Sherpa 2.2.4, Sherpa 2.2.11, MadGraph5_aMC@NLO+Pythia 8 (MG5_aMC+Pythia8 in the legend), and MiNNLO$_{\mathrm{PS}}$. Fixed-order calculation results from MATRIX NNLO are also shown. Dashed bands represent the statistical uncertainty and theoretical uncertainty (PDF and scale variations). The bottom panels show the ratio of the SM prediction to the measured cross section.

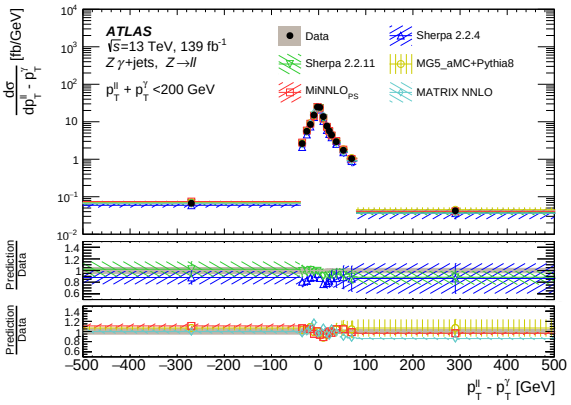

(a)

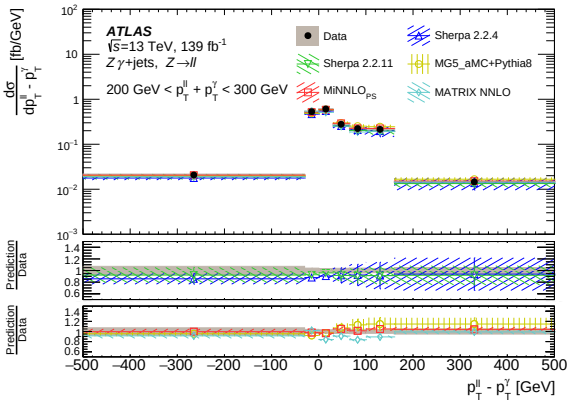

(b)

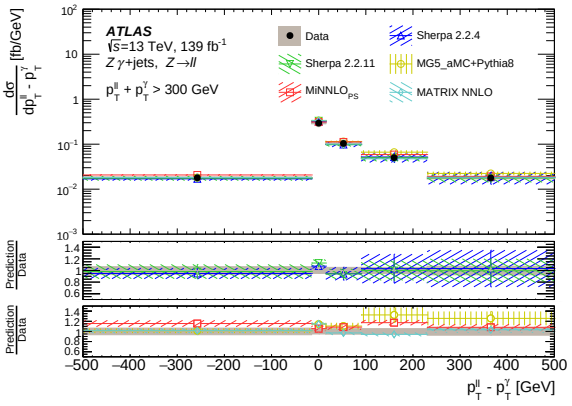

(c)

Figure 11: Measured differential cross section (black data points) as a function of $p_{\mathrm{T}}^{\ell\ell} - p_{\mathrm{T}}^{\gamma}$ (a) in $p_{\mathrm{T}}^{\ell\ell} + p_{\mathrm{T}}^{\gamma} < 200$ GeV, (b) in 200 GeV $< p_{\mathrm{T}}^{\ell\ell} + p_{\mathrm{T}}^{\gamma} < 300$ GeV, and (c) in $p_{\mathrm{T}}^{\ell\ell} + p_{\mathrm{T}}^{\gamma} > 300$ GeV. Error bands on the data points show the statistical uncertainty, while the grey area shows the total uncertainty in the unfolded result. Measured cross sections are compared with SM predictions from event generators at particle level: Sherpa 2.2.4, Sherpa 2.2.11, MadGraph5_aMC@NLO+Pythia 8 (MG5_aMC+Pythia8 in the legend), and MiNNLO$_{\mathrm{PS}}$. Fixed-order calculation results using MATRIX NNLO are also shown. Dashed bands represent the statistical uncertainty and theoretical uncertainty (PDF and scale variations). The bottom panels show the ratio of the SM prediction to the measured cross section.

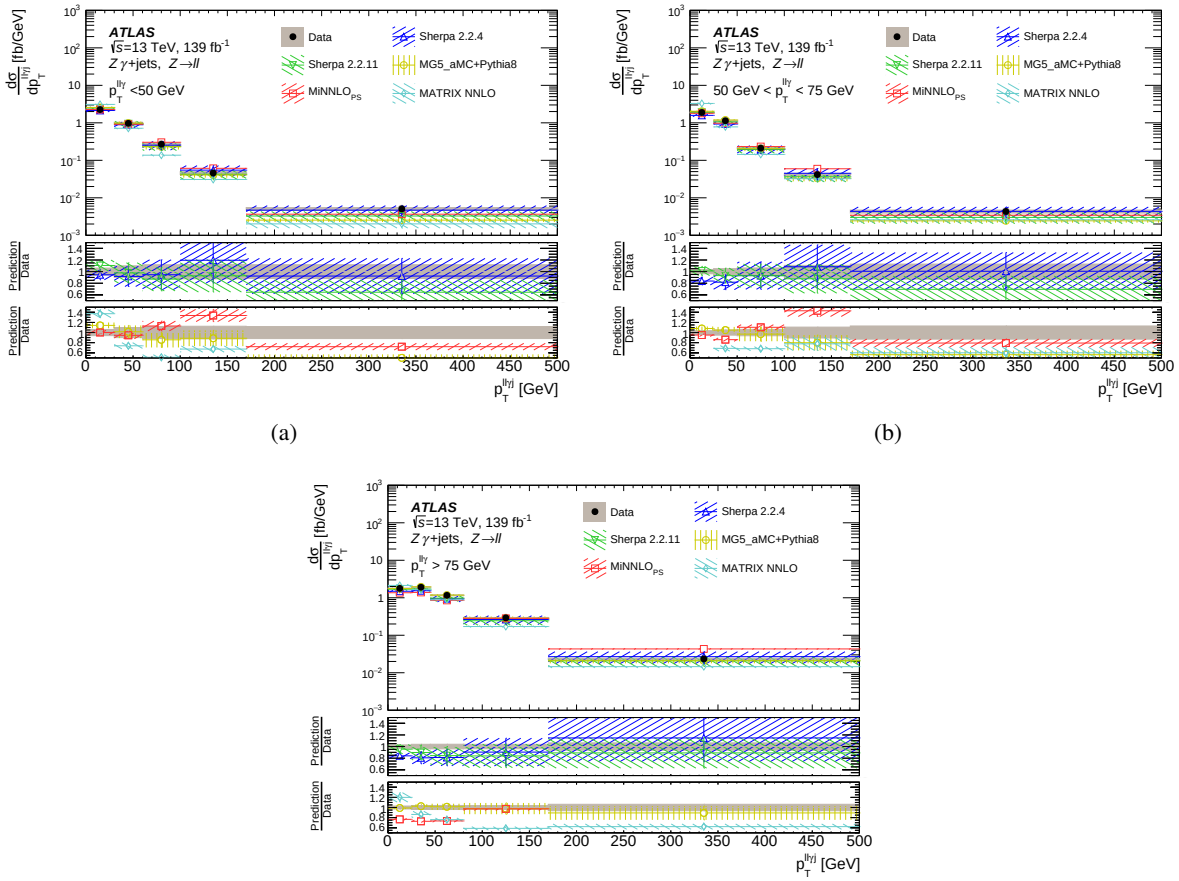

(a) (b)

(c)

Figure 12: Measured differential cross section (black data points) as a function of $p_{\mathrm{T}}^{\ell\ell\gamma\mathrm{j}}$ (a) in $p_{\mathrm{T}}^{\ell\ell\gamma} < 50$ GeV, (b) in 50 GeV $< p_{\mathrm{T}}^{\ell\ell\gamma} < 75$ GeV, and (c) in 75 GeV $< p_{\mathrm{T}}^{\ell\ell\gamma}$. Error bands on the data points show the statistical uncertainty, while the grey area shows the total uncertainty in the unfolded result. Measured cross sections are compared with SM predictions from event generators at particle level: Sherpa 2.2.4, Sherpa 2.2.11, MadGraph5_aMC@NLO+Pythia 8 (MG5_aMC+Pythia8 in the legend), and MiNNLO$_{\mathrm{PS}}$. Fixed-order calculation results from MATRIX NNLO are also shown. Dashed bands represent the statistical uncertainty and theoretical uncertainty (PDF and scale variations). The bottom panels show the ratio of the SM prediction to the measured cross section.

10 Conclusion

A measurement of several differential cross sections for $Z\gamma$ production in association with jets is presented, in the final state where the Z boson decays into two opposite-sign same-flavour leptons (e^+e^- or $\mu^+\mu^-$). The measurement is performed in a fiducial phase space enhanced in ISR photons, where the sum of the invariant mass of the leptons and the invariant mass of the leptons and the photon is greater than twice the mass of the Z boson. The measurement is performed using data collected by the ATLAS detector from LHC pp collisions at $\sqrt{s} = 13$ TeV, using a total integrated luminosity of 139 fb^{-1}.

Differential cross sections are measured as functions of the kinematics of jets, leptons, and photons. Both one-dimensional and two-dimensional distributions are chosen to enhance the separation of hard-scatter effects from soft collinear radiation. A precise measurement of $Z\gamma$ production in association with jets is obtained, with a total uncertainty between 4% and 10% depending on the number of jets. The results are compared with QCD predictions from MC generators involving different precision of multileg merging at LO and NLO, as well as recent predictions at NNLO, including from MiNNLO$_{\text{PS}}$, and fixed-order calculations such as with MATRIX. The predictions are in general in good agreement with the measurements. Jet activity is generally well described, but some trends are observed in the different predictions. Observables sensitive to polarisation effects of the Z boson are well modelled by all predictions. The measurements of $Z\gamma$ production in association with jets have the potential to constrain the QCD predictions and improve resummation calculations in regions where Sudakov-logarithm terms dominate.

References

[1] L. Evans and P. Bryant, *LHC Machine*, JINST **3** (2008) S08001.

[2] M. Wiesemann, L. Rottoli and P. Torrielli, *The Zγ transverse-momentum spectrum at NNLO+N3LL*, Phys. Lett. B **809** (2020) 135718, arXiv: 2006.09338 [hep-ph].

[3] R. D. Ball et al., *Parton distributions from high-precision collider data*, Eur. Phys. J. C **77** (2017), ISSN: 1434-6052, arXiv: 1706.00428 [hep-ph].

[4] J. Krause and F. Siegert, *NLO QCD predictions for $Z + \gamma + j$ production with Sherpa*, Eur. Phys. J. C **78** (2018), arXiv: 1708.06283 [hep-ph].

[5] M. A. Ebert and F. J. Tackmann, *Resummation of Transverse Momentum Distributions in Distribution Space*, JHEP **02** (2017) 110, arXiv: 1611.08610 [hep-ph].

[6] M. A. Ebert, J. K. L. Michel, I. W. Stewart and F. J. Tackmann, *Drell-Yan q_T resummation of fiducial power corrections at N^3LL*, JHEP **04** (2021) 102, arXiv: 2006.11382 [hep-ph].

[7] G. Lustermans, J. K. L. Michel, F. J. Tackmann and W. J. Waalewijn, *Joint two-dimensional resummation in q_T and 0-jettiness at NNLL*, JHEP **03** (2019) 124, arXiv: 1901.03331 [hep-ph].

[8] L3 Collaboration, *Study of the $e^+e^- \to Z\gamma$ process at LEP and limits on triple neutral-gauge-boson couplings*, Phys. Lett. B **597** (2004) 119, arXiv: hep-ex/0407012 [hep-ex].

[9] DELPHI Collaboration, *Study of triple-gauge-boson couplings ZZZ, ZZγ and Zγγ at LEP*, Eur. Phys. J. C **51** (2007) 525, arXiv: 0706.2741 [hep-ex].

[10] OPAL Collaboration, *Search for trilinear neutral gauge boson couplings in $Z\gamma$ production at $\sqrt{s} = 189$ GeV at LEP*, Eur. Phys. J. C **17** (2000) 553, arXiv: hep-ex/0007016 [hep-ex].

[11] D0 Collaboration, *$Z\gamma$ production and limits on anomalous $ZZ\gamma$ and $Z\gamma\gamma$ couplings in $p\bar{p}$ collisions at $\sqrt{s} = 1.96$ TeV*, Phys. Rev. D **85** (2012) 052001, arXiv: 1111.3684 [hep-ex].

[12] D0 Collaboration, *Measurement of the $Z\gamma \to \nu\bar{\nu}\gamma$ Production Cross Section and Limits on Anomalous $ZZ\gamma$ and $Z\gamma\gamma$ Couplings in $p\bar{p}$ Collisions at $\sqrt{s} = 1.96$ TeV*, Phys. Rev. Lett. **102** (2009) 201802, arXiv: 0902.2157 [hep-ex].

[13] ATLAS Collaboration, *Measurements of $Z\gamma$ and $Z\gamma\gamma$ production in pp collisions at $\sqrt{s} = 8$ TeV with the ATLAS detector*, Phys. Rev. D **93** (2016) 112002, arXiv: 1604.05232 [hep-ex].

[14] ATLAS Collaboration, *Measurement of the $Z(\to \ell^+\ell^-)\gamma$ production cross-section in pp collisions at $\sqrt{s} = 13$ TeV with the ATLAS detector*, JHEP **03** (2020) 054, arXiv: 1911.04813 [hep-ex].

[15] CMS Collaboration, *Measurement of the $Z\gamma$ production cross section in pp collisions at 8 TeV and search for anomalous triple gauge boson couplings*, JHEP **04** (2015) 164, arXiv: 1502.05664 [hep-ex].

[16] H. Georgi, D. B. Kaplan and L. Randall, *Manifesting the invisible axion at low energies*, Phys. Lett. B **169** (1986) 73, ISSN: 0370-2693.

[17] J. Preskill, M. B. Wise and F. Wilczek, *Cosmology of the Invisible Axion*, Phys. Lett. B **120** (1983) 127.

[18] S. Carra et al., *Constraining off-shell production of axion-like particles with $Z\gamma$ and WW differential cross-section measurements*, Phys. Rev. D **104** (2021) 092005, arXiv: 2106.10085 [hep-ex].

[19] M. B. Gavela, J. M. No, V. Sanz and J. F. de Trocóniz, *Nonresonant Searches for Axionlike Particles at the LHC*, Phys. Rev. Lett. **124** (2020), arXiv: 1905.12953 [hep-ph].

[20] I. Brivio and M. Trott, *The standard model as an effective field theory*, Physics Reports **793** (2019) 1, arXiv: 1706.08945 [hep-ph].

[21] E. Bothmann et al., *Event generation with Sherpa 2.2*, SciPost Phys. **7** (2019) 034, arXiv: 1905.09127 [hep-ph].

[22] J. Alwall et al., *The automated computation of tree-level and next-to-leading order differential cross sections, and their matching to parton shower simulations*, JHEP **07** (2014) 079, arXiv: 1405.0301 [hep-ph].

[23] P. F. Monni, P. Nason, E. Re, M. Wiesemann and G. Zanderighi, *MiNNLO$_{PS}$: a new method to match NNLO QCD to parton showers*, JHEP **05** (2020) 143, [Erratum: JHEP 02, 031 (2022)], arXiv: 1908.06987 [hep-ph].

[24] D. Lombardi, M. Wiesemann and G. Zanderighi, *Advancing MiNNLO$_{PS}$ to diboson processes: $Z\gamma$ production at NNLO+PS*, JHEP **06** (2021) 095, arXiv: 2010.10478 [hep-ph].

[25] M. Grazzini, S. Kallweit and M. Wiesemann, *Fully differential NNLO computations with MATRIX*, Eur. Phys. J. C **78** (2018) 537, arXiv: 1711.06631 [hep-ph].

[26] M. Grazzini, S. Kallweit and D. Rathlev, *$W\gamma$ and $Z\gamma$ production at the LHC in NNLO QCD*, JHEP **07** (2015) 085, arXiv: 1504.01330 [hep-ph].

[27] ATLAS Collaboration, *The ATLAS Experiment at the CERN Large Hadron Collider*, JINST **3** (2008) S08003.

[28] ATLAS Collaboration, *The ATLAS Collaboration Software and Firmware*, ATL-SOFT-PUB-2021-001, 2021, URL: https://cds.cern.ch/record/2767187.

[29] ATLAS Collaboration, *ATLAS data quality operations and performance for 2015–2018 data-taking*, JINST **15** (2020) P04003, arXiv: 1911.04632 [physics.ins-det].

[30] ATLAS Collaboration, *Luminosity determination in pp collisions at $\sqrt{s} = 13$ TeV using the ATLAS detector at the LHC*, ATLAS-CONF-2019-021, 2019, URL: https://cds.cern.ch/record/2677054.

[31] G. Avoni et al., *The new LUCID-2 detector for luminosity measurement and monitoring in ATLAS*, JINST **13** (2018) P07017.

[32] S. Höche, F. Krauss, M. Schönherr and F. Siegert, *A critical appraisal of NLO+PS matching methods*, JHEP **09** (2012) 049, arXiv: 1111.1220 [hep-ph].

[33] S. Höche, F. Krauss, M. Schönherr and F. Siegert, *QCD matrix elements + parton showers. The NLO case*, JHEP **04** (2013) 027, arXiv: 1207.5030 [hep-ph].

[34] S. Catani, F. Krauss, R. Kuhn and B. R. Webber, *QCD Matrix Elements + Parton Showers*, JHEP **11** (2001) 063, arXiv: hep-ph/0109231.

[35] S. Höche, F. Krauss, S. Schumann and F. Siegert, *QCD matrix elements and truncated showers*, JHEP **05** (2009) 053, arXiv: 0903.1219 [hep-ph].

[36] R. D. Ball et al., *Parton distributions for the LHC Run II*, JHEP **04** (2015) 040, arXiv: 1410.8849 [hep-ph].

[37] S. Frixione, *Isolated photons in perturbative QCD*, Phys. Lett. B **429** (1998) 369, arXiv: hep-ph/9801442.

[38] T. Gleisberg and S. Höche, *Comix, a new matrix element generator*, JHEP **12** (2008) 039, arXiv: 0808.3674 [hep-ph].

[39] S. Schumann and F. Krauss, *A parton shower algorithm based on Catani–Seymour dipole factorisation*, JHEP **03** (2008) 038, arXiv: 0709.1027 [hep-ph].

[40] R. D. Ball et al., *Parton distributions for the LHC run II*, JHEP **04** (2015) 040, arXiv: 1410.8849 [hep-ph].

[41] T. Sjöstrand, S. Mrenna and P. Skands, *A brief introduction to PYTHIA 8.1*, Comput. Phys. Commun. **178** (2008) 852, arXiv: 0710.3820 [hep-ph].

[42] P. Nason, *A New method for combining NLO QCD with shower Monte Carlo algorithms*, JHEP **11** (2004) 040, arXiv: hep-ph/0409146.

[43] S. Frixione, P. Nason and C. Oleari, *Matching NLO QCD computations with Parton Shower simulations: the POWHEG method*, JHEP **11** (2007) 070, arXiv: 0709.2092 [hep-ph].

[44] S. Alioli, P. Nason, C. Oleari and E. Re, *A general framework for implementing NLO calculations in shower Monte Carlo programs: the POWHEG BOX*, JHEP **06** (2010) 043, arXiv: 1002.2581 [hep-ph].

[45] S. Alioli, P. Nason, C. Oleari and E. Re, *NLO vector-boson production matched with shower in POWHEG*, JHEP **07** (2008) 060, arXiv: 0805.4802 [hep-ph].

[46] ATLAS Collaboration, *Measurement of the Z/γ^* boson transverse momentum distribution in pp collisions at $\sqrt{s} = 7$ TeV with the ATLAS detector*, JHEP **09** (2014) 145, arXiv: 1406.3660 [hep-ex].

[47] H.-L. Lai et al., *New parton distributions for collider physics*, Phys. Rev. D **82** (2010) 074024, arXiv: 1007.2241 [hep-ph].

[48] J. Pumplin et al., *New Generation of Parton Distributions with Uncertainties from Global QCD Analysis*, JHEP **07** (2002) 012, arXiv: hep-ph/0201195.

[49] T. Sjöstrand et al., *An introduction to PYTHIA 8.2*, Comput. Phys. Commun. **191** (2015) 159, arXiv: 1410.3012 [hep-ph].

[50] ATLAS Collaboration, *ATLAS Pythia 8 tunes to 7 TeV data*, ATL-PHYS-PUB-2014-021, 2014, URL: https://cds.cern.ch/record/1966419.

[51] K. Melnikov, M. Schulze and A. Scharf,
QCD corrections to top quark pair production in association with a photon at hadron colliders,
Phys. Rev. D **83** (2011) 074013, arXiv: 1102.1967 [hep-ph].

[52] D. de Florian et al.,
Handbook of LHC Higgs Cross Sections: 4. Deciphering the Nature of the Higgs Sector, (2016),
arXiv: 1610.07922 [hep-ph].

[53] F. Buccioni et al., *OpenLoops 2*, Eur. Phys. J. C **79** (2019) 866, arXiv: 1907.13071 [hep-ph].

[54] F. Cascioli, P. Maierhöfer and S. Pozzorini, *Scattering Amplitudes with Open Loops*,
Phys. Rev. Lett. **108** (2012) 111601, arXiv: 1111.5206 [hep-ph].

[55] A. Denner, S. Dittmaier and L. Hofer,
Collier: A fortran-based complex one-loop library in extended regularizations,
Comput. Phys. Commun. **212** (2017) 220, arXiv: 1604.06792 [hep-ph].

[56] ATLAS Collaboration, *The Pythia 8 A3 tune description of ATLAS minimum bias and inelastic measurements incorporating the Donnachie–Landshoff diffractive model*,
ATL-PHYS-PUB-2016-017, 2016, URL: https://cds.cern.ch/record/2206965.

[57] GEANT4 Collaboration, S. Agostinelli et al., *Geant4 – a simulation toolkit*,
Nucl. Instrum. Meth. A **506** (2003) 250.

[58] ATLAS Collaboration, *The ATLAS Simulation Infrastructure*, Eur. Phys. J. C **70** (2010) 823,
arXiv: 1005.4568 [physics.ins-det].

[59] S. Alioli, P. Nason, C. Oleari and E. Re, *A general framework for implementing NLO calculations in shower Monte Carlo programs: the POWHEG BOX*, JHEP **06** (2010) 043,
arXiv: 1002.2581 [hep-ph].

[60] T. Gehrmann and L. Tancredi, *Two-loop QCD helicity amplitudes for $q\bar{q} \to W^{\pm}\gamma$ and $q\bar{q} \to Z^0\gamma$*,
JHEP **02** (2012) 004, arXiv: 1112.1531 [hep-ph].

[61] S. Catani, L. Cieri, D. de Florian, G. Ferrera and M. Grazzini,
Vector boson production at hadron colliders: hard-collinear coefficients at the NNLO,
Eur. Phys. J. C **72** (2012) 2195, arXiv: 1209.0158 [hep-ph].

[62] S. Catani and M. Grazzini, *Next-to-Next-to-Leading-Order Subtraction Formalism in Hadron Collisions and its Application to Higgs-Boson Production at the Large Hadron Collider*,
Phys. Rev. Lett. **98** (2007) 222002, arXiv: hep-ph/0703012 [hep-ph].

[63] S. Dulat et al.,
New parton distribution functions from a global analysis of quantum chromodynamics,
Phys. Rev. D **93** (2016) 033006, arXiv: 1506.07443 [hep-ph].

[64] ATLAS Collaboration, *Performance of electron and photon triggers in ATLAS during LHC Run 2*,
Eur. Phys. J. C **80** (2020) 47, arXiv: 1909.00761 [hep-ex].

[65] ATLAS Collaboration, *Performance of the ATLAS muon triggers in Run 2*,
JINST **15** (2020) P09015, arXiv: 2004.13447 [hep-ex].

[66] ATLAS Collaboration, *Electron and photon performance measurements with the ATLAS detector using the 2015–2017 LHC proton–proton collision data*, JINST **14** (2019) P12006,
arXiv: 1908.00005 [hep-ex].

[67] ATLAS Collaboration, *Muon reconstruction and identification efficiency in ATLAS using the full Run 2 pp collision data set at* $\sqrt{s} = 13$ *TeV*, Eur. Phys. J. C **81** (2021) 578, arXiv: 2012.00578 [hep-ex].

[68] ATLAS Collaboration, *Measurement of the inclusive isolated prompt photon cross section in pp collisions at* $\sqrt{s} = 8$ *TeV with the ATLAS detector*, JHEP **08** (2016) 005, arXiv: 1605.03495 [hep-ex].

[69] ATLAS Collaboration, *Measurement of the photon identification efficiencies with the ATLAS detector using LHC Run 2 data collected in 2015 and 2016*, Eur. Phys. J. C **79** (2019) 205, arXiv: 1810.05087 [hep-ex].

[70] M. Cacciari, G. P. Salam and G. Soyez, *The anti-*k_t *jet clustering algorithm*, JHEP **04** (2008) 063, arXiv: 0802.1189 [hep-ph].

[71] M. Cacciari, G. P. Salam and G. Soyez, *FastJet user manual*, Eur. Phys. J. C **72** (2012) 1896, arXiv: 1111.6097 [hep-ph].

[72] ATLAS Collaboration, *Jet reconstruction and performance using particle flow with the ATLAS Detector*, Eur. Phys. J. C **77** (2017) 466, arXiv: 1703.10485 [hep-ex].

[73] ATLAS Collaboration, *Jet energy scale and resolution measured in proton–proton collisions at* $\sqrt{s} = 13$ *TeV with the ATLAS detector*, Eur. Phys. J. C **81** (2020) 689, arXiv: 2007.02645 [hep-ex].

[74] ATLAS Collaboration, *Performance of pile-up mitigation techniques for jets in pp collisions at* $\sqrt{s} = 8$ *TeV using the ATLAS detector*, Eur. Phys. J. C **76** (2016) 581, arXiv: 1510.03823 [hep-ex].

[75] W. J. Stirling and E. Vryonidou, *Electroweak gauge boson polarisation at the LHC*, JHEP **07** (2012) 124, arXiv: 1204.6427 [hep-ph].

[76] J. C. Collins and D. E. Soper, *Angular Distribution of Dileptons in High-Energy Hadron Collisions*, Phys. Rev. D **16** (1977) 2219.

[77] CMS Collaboration, *Angular coefficients of Z bosons produced in pp collisions at* $\sqrt{s} = 8$ *TeV and decaying to* $\mu^+\mu^-$ *as a function of transverse momentum and rapidity*, Phys. Lett. B **750** (2015) 154, arXiv: 1504.03512 [hep-ex].

[78] ATLAS Collaboration, *Measurement of* $W^\pm Z$ *production cross sections and gauge boson polarisation in pp collisions at* $\sqrt{s} = 13$ *TeV with the ATLAS detector*, Eur. Phys. J. C **79** (2019) 535, arXiv: 1902.05759 [hep-ex].

[79] ATLAS Collaboration, *Measurement of the inclusive isolated prompt photon cross section in pp collisions at* $\sqrt{s} = 7$ *TeV with the ATLAS detector*, Phys. Rev. D **83** (2011) 052005, arXiv: 1012.4389 [hep-ex].

[80] ATLAS Collaboration, *Measurements of inclusive and differential fiducial cross-sections of* $t\bar{t}\gamma$ *production in leptonic final states at* $\sqrt{s} = 13$ *TeV in ATLAS*, Eur. Phys. J. C **79** (2019) 382, arXiv: 1812.01697 [hep-ex].

[81] G. D'Agostini, *A multidimensional unfolding method based on Bayes' theorem*, Nucl. Instrum. Methods. Phys. Res. A **362** (1995) 487, ISSN: 0168-9002.

[82] ATLAS Collaboration, *Jet energy scale and resolution measured in proton–proton collisions at* $\sqrt{s} = 13$ *TeV with the ATLAS detector*, Eur. Phys. J. C **81** (2021) 689, arXiv: 2007.02645 [hep-ex].

[83] B. Efron, *Bootstrap Methods: Another Look at the Jackknife*, Annals Statist. **7** (1979) 1, arXiv: 1706.00428 [hep-ph].

[84] J. Butterworth et al., *PDF4LHC recommendations for LHC Run II*, J. Phys. G: Nucl. Part. Phys. **43** (2016) 023001, ISSN: 1361-6471, arXiv: 1510.03865 [hep-ph].

[85] ATLAS Collaboration, *Measurements of $W^+W^-+ \geq 1$ jet production cross-sections in pp collisions at $\sqrt{s} = 13$ TeV with the ATLAS detector*, JHEP **06** (2021) 003, arXiv: 2103.10319 [hep-ex].

[86] ATLAS Collaboration, *Studies of $Z\gamma$ production in association with a high-mass dijet system in pp collisions at $\sqrt{s} = 8$ TeV with the ATLAS detector*, JHEP **07** (2017) 107, arXiv: 1705.01966 [hep-ex].